Agricultural and Forest Meteorology 342 (2023) 109687

Contents lists available at ScienceDirect

Agricultural and Forest Meteorology

journal homepage: www.elsevier.com/locate/agrformet

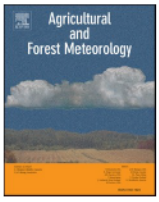

The role of surface energy fluxes in determining mixing layer heights

Eric R. Beamesderfer [a,b,c,*], Sebastien C. Biraud [d], Nathaniel A. Brunsell [e], Mark A. Friedl [f], Manuel Helbig [g], David Y. Hollinger [h], Thomas Milliman [i], David A. Rahn [e], Russell L. Scott [j], Paul C. Stoy [k], Jen L. Diehl [a,b], Andrew D. Richardson [a,b]

[a] Center for Ecosystem Science and Society, Northern Arizona University, Flagstaff, AZ, United States
[b] School of Informatics, Computing & Cyber Systems, Northern Arizona University, Flagstaff, AZ, United States
[c] Department of Atmospheric Science, University of Wyoming, Laramie, WY, United States
[d] Climate Sciences Department, Lawrence Berkeley National Laboratory, Berkeley, CA, United States
[e] Department of Geography and Atmospheric Science, University of Kansas, Lawrence, KS, United States
[f] Department of Earth and Environment, Boston University, Boston, MA, United States
[g] Department of Physics and Atmospheric Science, Dalhousie University, Halifax, NS, Canada
[h] Northern Research Station, USDA Forest Service, Durham, NH, United States
[i] Earth Systems Research Center, University of New Hampshire, Durham, NH, United States
[j] Southwest Watershed Research Center, USDA-ARS, Tucson, AZ, United States
[k] Department of Biological Systems Engineering, University of Wisconsin-Madison, Madison, WI, United States

ARTICLE INFO

Keywords:
Land-atmosphere interactions
Boundary layer height
Surface energy budget
Eddy-covariance
Phenology
AmeriFlux

ABSTRACT

The atmospheric mixing layer height (MLH) is a critical variable for understanding and constraining ecosystem and climate dynamics. Past MLH estimation efforts have largely relied on data with low temporal (radiosondes) or spatial (reanalysis) resolutions. This study is unique in that it utilized continuous point-based ceilometer- and radiosonde-derived measurements of MLH at surface flux tower sites to identify the surface influence on MLH dynamics. We found a strong correlation (R^2 = 0.73-0.91) between radiosonde MLH and ceilometer MLH at two sites with co-located observations. Seasonally, mean MLH was the highest at all sites during the summer, while the highest annual mean MLH was found at the warm and dry sites, dominated by high sensible heat fluxes. At daily time scales, surface fluxes of sensible heat, latent heat, and vapor pressure deficit had the largest influence on afternoon MLH. However, at best, the identified forcing variables and surface fluxes only accounted for ~38-65% of the variability in MLH under all sky conditions, and ~53-76% of the variability under clear skies. These results highlight the difficulty in using single-point observations to explain MLH dynamics but should encourage the use of ceilometers or similar atmospheric measurements at surface flux sites in future studies.

1. Introduction

The atmospheric boundary layer (ABL) is the lowest layer of the atmosphere that is in direct contact with the Earth's surface. The ABL is a critical component of the Earth's climate system as processes within the ABL control the exchange of energy, mass, momentum, and pollutants between the land surface and the atmosphere (Seibert, 2000; Stull, 1988; Yi, 2004). The height and structure of the ABL can be highly variable within a day and between seasons as it is influenced by diurnal and seasonal variations in the surface energy budget, incoming solar radiation, free atmospheric temperature and humidity profiles, and synoptic weather systems (Helbig et al., 2021; Zilitinkevich et al., 2012). Gaseous or particulate substances emitted from the surface become well mixed within the ABL due to turbulent mixing from buoyant convection and/or wind shear (Schween et al., 2014). This well-mixed layer, also known as the mixing layer, can grow up to several kilometers, bounded by the land surface below and a capping temperature inversion or statically stable layer of air above (Kotthaus and Grimmond, 2018; Wouters et al., 2019). The resulting mixing layer height (MLH) is a critical variable for understanding and constraining ecosystem and climate dynamics as it directly affects the heat capacity of the ABL (Panwar et al., 2019), CO_2 concentrations within the ABL (Yi et al., 2001), the onset of convective precipitation events (Siqueira et al., 2009), and air pollutant (aerosol) dispersion and deposition (Seibert,

* Corresponding author.
E-mail address: ebeamesd@uwyo.edu (E.R. Beamesderfer).

https://doi.org/10.1016/j.agrformet.2023.109687
Received 5 August 2022; Received in revised form 29 June 2023; Accepted 25 August 2023

2000; Yin et al., 2019), among many other processes and interactions.

The most common methods to determine MLH examine deviations in vertical profiles of temperature, humidity, or Richardson number (Piringer et al., 2007; Seibert, 2000). These variables are often calculated using radiosonde data, but are commonly only used as a reference value, due to their limited (non-continuous) temporal resolution (Kotthaus and Grimmond, 2018; Münkel et al., 2007; Seidel et al., 2012). The lack of high temporal resolution radiosonde measurements can be resolved by incorporating continuous, ground-based proximal sensing techniques such as sodar, radar, and LiDAR instrumentation (Schween et al., 2014). These instruments are regarded as the most advanced methods for observing MLH, as they operate at a high temporal resolution and require minimal maintenance (Helbig et al., 2021). Aerosol backscatter LiDARs, also known as ceilometers, are single-lens and eye-safe LiDARs that were originally designed to measure cloud ceilings, but also provide a backscatter profile used for the determination of the MLH (Wiegner et al., 2014). Ceilometers have been utilized in many studies to estimate and evaluate the MLH (Caicedo et al., 2020; Emeis et al., 2008; Eresmaa et al., 2006; Gierens et al., 2019; Haeffelin et al., 2012; Hicks et al., 2019; Lotteraner and Piringer, 2016; Mues et al., 2017; Schween et al., 2014) as they offer one of the best proximal sensing options for the observation of atmospheric aerosols. However, when considering ecosystem-level analyses of MLH, recent studies have exclusively used modeled MLH outputs (e.g., Butterworth et al, 2021; Perkins, 2020; Schmiedeler, 2019), while limited research has analyzed ceilometer-derived MLH. Furthermore, diurnal and seasonal MLH dynamics are tightly coupled to surface fluxes of sensible and latent heat (Baldocchi and Ma, 2013; Betts, 2004; Yi et al., 2001), yet despite the close relation between surface fluxes and MLH, direct surface flux observations have rarely been analyzed together with MLH observations from ceilometers.

Airports, weather services, and global research institutions use ceilometers to examine cloud and MLH dynamics (e.g., heights and frequencies), but these observations are rarely located near continuous land-atmosphere (e.g., ecosystem meteorology and flux) monitoring stations. The AmeriFlux and global FLUXNET networks are an extensive system of eddy covariance (EC) flux tower sites that support continuous monitoring of energy, carbon, water, and other land-atmosphere fluxes (Baldocchi et al., 2001; Novick et al., 2018). The EC technique allows continuous, high frequency measurements of the surface turbulent fluxes of latent and sensible heat to be made, which among other mechanisms, are shown to be a primary driver of the growth of the ABL and MLH (Garratt, 1994; Stull, 1988). At present, MLH measurements are only made at a small number of flux sites worldwide, and these data are often not publicly available (Helbig et al., 2021). Consequently, this study is the first of its kind to incorporate co-located EC flux and ceilometer data for a range of sites across the United States, with the goal of answering the questions: (1) how do the MLH and flux relationships vary across season and ecosystem type, and (2) can we explain the day-to-day variations in MLH as a function of site-level environmental variables and fluxes?

In this study, we incorporate a range of neighboring (30 km) observations from radiosondes, ceilometers, flux towers, and reanalysis data to examine the direct influence of surface fluxes and the indirect influence of surface flux proxies on MLH dynamics at select US AmeriFlux sites. The specific goals of this research are to: (1) evaluate ceilometer-derived MLH retrievals against radiosonde-derived MLH estimates, (2) characterize MLH across various ecosystems and climates, (3) analyze the role of seasonal surface fluxes and phenology on MLH dynamics, and (4) examine the relative influence of explanatory variables on MLH at each site.

2. Methods and materials

2.1. Site selection and details

This study examined the relationships between ceilometer-derived (LiDAR; see section 2.2.2 for additional details) cloud and MLH data and EC flux and meteorological data for five AmeriFlux sites (Table 1, see also ameriflux.lbl.gov). These sites were included as they all had ceilometer measurements in close proximity to an active AmeriFlux site. Two of the sites (US-Wkg and US-Whs) shared a centrally located ceilometer due to their distance between each other (8 km apart) and were the only sites to not have co-located ceilometer and flux measurements (Table 1). The five sites span a climatological gradient across the United States and cover an area ranging from the cool and wet climate of Maine to the hot and arid climate of Arizona (Fig. 1). Additionally, the sites are composed of four main plant functional types (PFTs): evergreen needleleaf forests, grasslands, croplands, and open shrublands. The broad range of climates and PFTs in this study (Table 1) allows us to compare the seasonal patterns of MLH that may exist across different vegetation types.

The Howland Forest (US-Ho1) in Howland, Maine is a mature, multi-aged evergreen dominated forest (90% of trees) that has been unmanaged for nearly a century (Hollinger et al., 2021). The climate at US-Ho1 is hemiboreal (*Dfb;* Koppen climate classification), with long, cold winters, and warm summers. The Kansas Field Station (US-KFS) in Lawrence, Kansas is a heterogeneous grassland comprised of a mixture of C3 and some native C4 grasses (Brunsell et al., 2011). Infrequent (about every five years) prescribed burns occurred at the site prior to the EC installation in 2007, helping to maintain the site as a grassland. The Southern Great Plains (US-ARM) site located in Lamont, Oklahoma, part of the Department of Energy (DOE) Atmospheric Radiation Measurement (ARM) user facility (arm.gov) is covered by areas of winter wheat, grassland pastures, and some row-crop agriculture (Bagley et al., 2017; Fischer et al., 2007). The climate at US-KFS and US-ARM is warm temperate (*Cfa*) with hot and humid summers and mild winters. The remaining two sites, the Kendall Grassland (US-Wkg) and the Lucky Hills Shrubland (US-Whs), are located within the US Department of Agriculture Agricultural Research Service (USDA-ARS) Walnut Gulch Experimental Watershed (WGEW) near Tombstone, Arizona. The desert shrubland (US-Whs) is dominated by shrubs, with nearly no grass presence at the site, while the grassland (US-Wkg) is largely perennial bunchgrass (Scott et al., 2015, 2010). Both US-Wkg and US-Whs experience a cold semi-arid climate (*Bsk*) due to their elevation (1370 1530 m above sea level), with cold winters and hot summers, and the majority of their rainfall falling from July to September. The geographic distribution of sites is shown in Fig. 1, with additional information found at their respective DOIs (Table 1).

2.2. Data descriptions

2.2.1. Theory and data selection

The complex process-level relationships and feedbacks between surface fluxes and the MLH are an important topic of research (Santanello et al., 2018). Therefore, we highlight these interactions to provide an overview of the observations used throughout this study. The surface energy balance describes the bi-directional exchange and partitioning of energy fluxes toward and away from the surface and is inseparably linked to the overlying mixing layer. Strong surface heating can positively influence MLH growth, especially over dry soils, while increases in the amount of surface evaporation and a concurrent reduction in surface sensible heat flux, often over wetter soils, may act to limit the growth of the MLH (Santanello et al., 2018; Yi et al., 2004). This exchange of energy directly influences the air temperature and humidity profiles within the ABL as well as the temperature of the surface (Jin and Dickinson, 2010; Konings et al., 2010). However, varying hydroclimatic regimes, PFTs, and atmospheric stability conditions are shown to influence the

Table 1
Metadata for the AmeriFlux sites used in this study. Site mean annual temperature (MAT; °C) and mean annual precipitation (MAP; mm) are the 30-year mean values reported on the AmeriFlux site webpages. Additional site information can be found at the respective DOIs.

Site	IGBP*	Latitude	Longitude	MAT	MAP	Years	Distance	Ceilometer	DOI%
US-Ho1	ENF	45.20	-68.74	5.3	1070	2013 – 2019	On-Site	Vaisala CL31	1246061
US-KFS	GRA	39.06	-95.19	12.0	1014	2016 – 2019	On-Site	Vaisala CL51	1246132
US-ARM	CRO	36.61	-97.49	14.8	843	2012 – 2020	On-Site	Vaisala CL31	1246027
US-Wkg	GRA	31.74	-109.94	15.6	407	2017 – 2020	11 km	Lufft CHM15k	1246112
US-Whs	OSH	31.75	-110.05	17.6	320	2017 – 2020	3 km		1246113

* IGBP Vegetation Classifications: ENF, Evergreen Needleleaf Forest; CRO, Croplands; GRA, Grasslands; and OSH, Open Shrublands. %DOI: AmeriFlux DOIs are preceded by '10.17190/AMF/'.

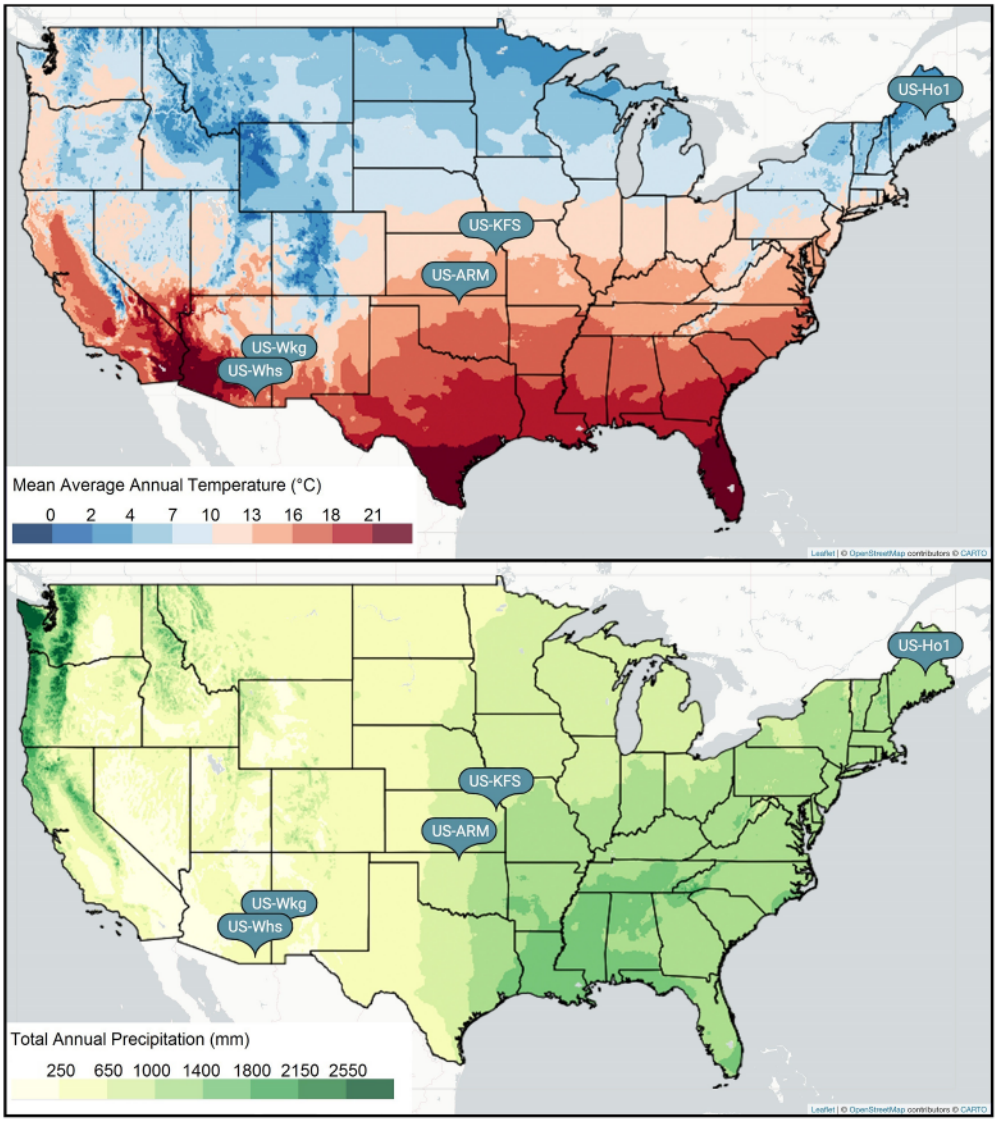

Fig. 1. The geographic distribution of the AmeriFlux sites including the 30-year (1991-2020) mean (a) annual temperature (MAT) and (b) annual precipitation (MAP) for the United States (NOAA NCEI). Site-specific values and additional information are listed in Table 1.

strength of these relationships on influencing MLH (Baldocchi and Ma, 2013; Findell and Eltahir, 2003; Koster et al., 2009), which also depends in part on vegetation structure and function. Consequently, to capture and characterize the role of surface processes in controlling MLH, this study included measurements of: (1) sensible heat flux (H, W m^{-2}) and (2) latent heat flux (LE, W m^{-2}) which act as direct drivers of MLH, and indirect drivers such as (3) vapor pressure deficit (VPD, kPa), (4) 5-10 cm (near-surface) soil water content (θ_{10cm}, m^3 m^{-3}), (5) the difference (T_{diff}, °C) between the air temperature (T_a, °C) and radiometric surface temperature (T_{sfc}, °C), (6) PhenoCam greenness chromatic coordinate (Gcc), and (7) the low-level humidity index (HI_{Low}, °C). All site-level data were averaged to provide a singular daily daytime value (here defined as 8 am to 6 pm local standard time).

2.2.2. Eddy covariance and phenology data

Half-hourly fluxes of LE, H, and meteorological data from each site were downloaded directly from the open-access AmeriFlux website. Missing data of all lengths (often due to instrument failure or

malfunction) were gap-filled using *REddyProc* (Wutzler et al., 2018). *REddyProc* relies on half-hourly measurements of the net ecosystem exchange (NEE) of CO_2, T_a, or soil temperature (T_s), incoming shortwave radiation (R_g), and VPD, to fill the gaps in the half-hourly EC data. Many sites do not report VPD, in which case VPD was calculated from measured relative humidity (RH) and T_a data (Campbell and Norman, 1998). *REddyProc* estimates a site-specific u* threshold (Papale et al., 2006) before filtering out periods of low turbulent mixing (u* filtering). After low-turbulence periods are removed, data gaps were filled using a combination of look-up tables, mean diurnal course, or marginal distribution sampling methods (Wutzler et al., 2018).

Following the completion of the *REddyProc* processing, continuous half-hourly gap-filled flux and meteorological data were available at each of the sites. From here, we calculated the radiometric surface temperature (T_{sfc}) using the *BigLeaf* R package (Knauer et al., 2018):

$$((\qquad)/ \quad) \tag{1}$$

where LW_{up} and LW_{down} are the flux tower measured upward and downward longwave radiation (W m ^{2}), respectively, is the emissivity of the surface (set to the commonly assumed value of 0.98), and is the Stefan-Boltzmann constant (5.67 10 ^{8} W m ^{2} K ^{4}). The T_a and T_{sfc} at a given site are strongly coupled and also sensitive to vegetation structure (e.g., aerodynamic roughness), which may lead to different responses between the T_a and T_{sfc} under varying evaporative conditions (Panwar et al., 2019). Therefore, we used the difference (T_{diff} T_a T_{sfc}) to better understand the relationships between the turbulent exchange of surface energy fluxes (across different vegetation types) and the atmosphere.

Canopy greenness data from the PhenoCam network (phenocam.nau.edu/webcam) were also included at each site to consider daily estimates of vegetation activity (phenology). The PhenoCam data were obtained from the PhenoCam V2 public data release (Seyednasrollah et al., 2019), and provide site-level estimates of canopy greenness from digital camera imagery. We quantified canopy greenness using Gcc, a commonly-used vegetation index (Richardson, 2019) which has been shown to be robust to changes in weather and illumination geometry. Gcc is calculated from the mean digital number (DN) of each of the red, green, blue (R_{DN}, G_{DN}, B_{DN}) colors across a masked region within each image, with the mask delineating the vegetation of interest:

$$\_\_\_\_\_ \tag{2}$$

Further details about the PhenoCam network and related data can be found in Richardson (2019).

2.2.3. Ceilometer data

Three of the five sites utilized a Vaisala (CL31 or CL51) ceilometer, while a Lufft CHM15k was used at the Arizona sites (US-Wkg and US-Whs) (Table 1). The Vaisala CL31 (CL51) records clouds and backscatter profiles up to a height of 7.5 km (15 km) at a temporal resolution of 2 s (6 s) and a vertical resolution of 10 m (10 m). The CL51 is listed to have an increased (up to 6 times greater) signal-to-noise ratio as compared to the CL31 (Morris and Winston, 2016). The Lufft CHM15k measures clouds and backscatter profiles up to 15 km, (like the Vaisala CL51) and has temporal and vertical resolutions of 15 s and 15 m, respectively.

All ceilometers retrieve MLH using the negative gradient of the aerosol backscatter profile and provide up to three levels of MLH attributions at each time step. For this analysis, we used the lowest detectable MLH returned by each ceilometer. For the Vaisala ceilometers, high resolution data were processed using the Vaisala BL-VIEW software, providing half-hourly estimates of MLH from the backscatter profiles (Münkel et al., 2011). For the Lufft CHM15k, no additional post-processing steps (e.g., BL-VIEW) were necessary to create the netCDF output files. The CHM15k at US-Wkg/Whs often failed to produce reasonable MLH outputs during the day, possibly due to low signal-to-noise ratios (Eresmaa et al., 2006; Kotthaus and Grimmond, 2018; Wiegner et al., 2014) or other factors, so the STRATfinder algorithm was also incorporated at those two sites (Kotthaus et al., 2020). The STRATfinder algorithm (written in MATLAB) combines STRAT-2-D/STRAT (Haeffelin et al., 2012) and pathfinderTURB (Poltera et al., 2017) to examine and trace daytime ceilometer-derived backscatter profiles for regions of significant vertical gradients, indicative of layer boundaries (e.g., mixing layer vs free atmosphere), in order to provide an optimized/idealized path of MLH at 1 min resolutions (Kotthaus et al., 2020).

Additionally, under conditions with significant clouds, precipitation, or adverse weather conditions, the estimate of MLH is highly uncertain or often poorly constrained. Therefore, the quality index and sky condition of the data were also evaluated and MLH data were removed if they did not meet the highest quality standards. For the Vaisala ceilometers, this study included MLH data with a *'bl_index_1* or quality index of 3, and for the Lufft ceilometer, a *'Q-Index* equal to 1 or 2. From these high quality half-hourly data, a late-afternoon (3 pm 7 pm local standard time) median MLH was calculated in order to produce maximum daily MLH (growth) estimates. Lastly, in the final part of this study, we considered only clear sky or 'cloud free data to analyze the highest quality MLH data at each site. Following the guidance of Oliphant et al. (2011), the half-hourly ceilometer cloud fractions were used to distinguish 'cloud free (20% of samples detecting clouds) conditions from cloudy or mixed sky conditions. When considering only daytime data (to not incorrectly characterize days with clouds present overnight), fewer than 6 daytime half-hours were required to be flagged as cloudy or mixed sky conditions for the day to be considered clear or 'cloud-free . All ceilometer data were recorded by default in UTC (coordinated universal time) and were adjusted to local time for the analysis and Fig.s.

2.2.4. Radiosondes and reanalysis data

Atmospheric sounding data were obtained from the University of Wyoming Department of Atmospheric Science (weather.uwyo.edu/upperair/sounding.html). The sounding data, measured at roughly 5-millibar (mb) vertical resolutions, correspond to atmospheric data from the National Weather Service (NWS) office nearest to the AmeriFlux tower (and location of each ceilometer). In some cases (US-Ho1 and US-Wkg/Whs), the nearest NWS office (often at an airport) was more than 80 km from the flux site, deemed to likely be unrepresentative of the site measurements. In other cases (US-KFS and US-ARM), the NWS radiosondes were launched within 30 km of the flux sites. At US-ARM, high vertical resolution (1 mb or hPa) DOE radiosondes were launched on-site and were used in this analysis. This study estimated MLH once daily using 00 UTC sounding data. Since the maximum MLH is estimated to occur in the mid-to-late afternoon (Seidel et al., 2010), we make the assumption that the 00 UTC (5 7 pm local standard time) sounding data most effectively estimates the maximum MLH for our North American site locations. MLH were estimated using the gradient method (Holzworth, 1967; Stull, 1988), which identifies vertical gradients of virtual potential temperature ($_v$, K) and specific humidity (q, g kg ^{1}) profiles. In a well-mixed layer (below the MLH), $_v$ and q remain constant with height (due to sufficient turbulent mixing). Consequently, this method defines the MLH as the height where $_v$ and q deviate from their near constant values, which is also where the gradient of $_v$ (q) is at a maximum (minimum), typical of the shift from a less stable region (the mixing layer) below the detected MLH to a more stable region (free troposphere) above the MLH (Seidel et al., 2010). While the NWS radiosondes effectively measure point-scale atmospheric profiles of wind, temperature, and moisture, regional reanalysis products may also be useful for locations where nearby in-situ measurements are limited (such as US-Ho1 and US-Wkg/Whs). Therefore, this analysis also included temperature, pressure, specific humidity, and PBL height (PBLH) data from the National Centers for Environmental Prediction

(NCEP) North American Regional Reanalysis (NARR) datasets at the grid point nearest (~32 km resolution) to each site during the study period. NCEP NARR data integrates national surface observations with model simulations to generate 3-hourly gridded datasets at 29 pressure levels ranging from the surface (~1000 hPa) up to 100 hPa (Mesinger et al., 2006). We used NARR products to: (1) compare the PBLH data to ceilometer MLH data for further confidence in the ceilometer data, and to (2) calculate low-level vertical profiles of air and dewpoint temperatures (T_d, °C) to determine the low-level humidity index (HI_{Low}), a measure of the preexisting moisture content of the lower atmosphere:

$$HI_{Low} = (Ta_{950} - Td_{850}) + (Ta_{850} - Td_{850}) \quad (3)$$

which calculates the dewpoint depressions ($T_a - T_d$) at 950 and 850 mb, or more generally, the sum of the dewpoint depressions at 50 and 100 mb above the ground surface (Findell and Eltahir, 2003). For this calculation, early morning (12 UTC) data were used, as suggested in the original framework. Since the HI_{Low} values were derived from reanalysis data, we then looked to quantify their accuracy and reliability. We calculated the total 9-year (2012 – 2020) daily HI_{Low} using radiosonde data, NARR data, and (a comparative reanalysis data product) the European Centre for Medium-Range Weather Forecasts (ECMRWF) fifth generation reanalysis data (ERA5) at the Southern Great Plains site (US-ARM); the only site in this study that had co-located flux, ceilometer, and radiosonde measurements. Fig. 2 shows how the HI_{Low} calculated using the ERA5 and NARR products are highly correlated across a wide range of HI_{Low} ($R^2 = 0.88$), but especially at the lowest HI_{Low} values (Fig. 2a). Similar results were found when comparing the radiosonde HI_{Low} to the NARR HI_{Low} ($R^2 = 0.86$; Fig. 2b). In both examples, the largest anomalies were found at high HI_{Low} values, indicative of a very dry lower atmosphere (Findell and Eltahir, 2003). While these findings helped us to trust the data at US-ARM and US-KFS (not shown but similar R^2), we acknowledge that using reanalysis data at other sites (with sparse surface observations) may not be illustrative of the actual HI_{Low}.

2.3. Boosted regression tree (BRT) analysis

The final portion of this analysis used boosted regression trees to quantify the "relative influence" of the outlined explanatory variables on ceilometer MLH at each site; implemented with the *gbm* package in the R computing environment (Elith et al., 2008; Ridgeway et al., 2020). We note that the relative influence, a metric estimated using the BRT method, is only indicative of correlation or association between MLH and the explanatory variables. Seasonal BRT models were constructed (based on calendar season), comprised of 100 BRTs each, and allowed for a direct comparison of the relationships between MLH and the explanatory variables. Training datasets (2/3 of the data) were incorporated for the BRTs to ensure distinct training and testing datasets, and to help assess each model's predictive power in estimating MLH. Using this methodology, the relative influence of the explanatory variables was calculated by summing the number of times a variable was chosen in a BRT, weighted by the BRT improvement of each partition. At each stage of the sequence, each data case is modeled from the current sequence of trees, and the prediction results are used as weights for fitting the next tree of the sequence (De'ath, 2007). The mean and standard deviation of the relative influence values from the 100 BRT model runs were plotted for assessment. Additionally, bin-averaged and partial dependence plots were used to capture the potential relationships between the explanatory and response variables (Friedman, 2001). This study presents the results found by calculating and comparing the seasonal relative influence of explanatory variables on ceilometer afternoon median MLH.

3. Results

3.1. Radiosonde MLH detection

The first objective of this research was to evaluate the quality of the ceilometer MLH retrievals at each site by comparing those data to the MLH derived from local radiosonde data. Since local surface properties influence atmospheric profiles of both temperature and humidity, we found poor relationships ($R^2 < 0.20$) between ceilometer MLH and

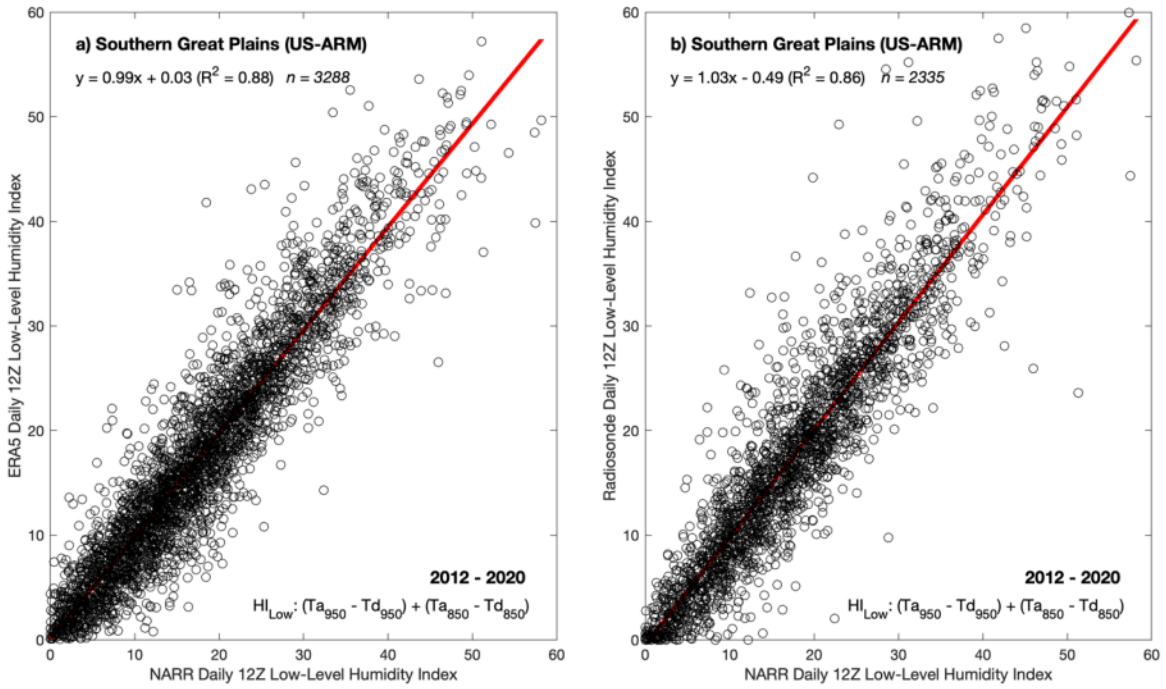

Fig. 2. Comparisons of the HI_{Low} calculations at the Southern Great Plains AmeriFlux site (US-ARM) from 2012 to 2020 between (a) the ERA5 and NARR data, and (b) the on-site radiosonde balloon sounding and NARR data. Fit equations and correlations are also shown.

radiosonde MLH at sites (e.g., US-Ho1 and US-Wkg/Whs) with large distances separating the two measurements. On the other hand, the relationships were substantially stronger for the two sites (US-KFS and US-ARM) where the concurrent measurements were made less than 30 km apart, shown in Fig. 3. At these sites, the data covering all seasons highlights that there is a strong positive correlation (thick red line) that is weakened by the lowest quality data (Index 1; orange line); where MLH estimates are highly uncertain. Conversely, the correlations increase at both sites with increasing data quality (derived from the ceilometer; blue and green lines). When only considering the highest quality data (Index 3; green line), there is a strong correlation at US-KFS (R^2 = 0.73; Fig. 3a) and at US-ARM (R^2 = 0.91; Fig. 3b), as the measurements at the latter are higher-resolution (vertically) and co-located. These relationships (Fig. 3) gave us confidence that the highest quality ceilometer MLH data, between 28% and 45% of all data measured at each site (Table 2), are in good agreement with the radiosonde data.

Table 2
(Top) The total percent of data contained within each quality index bin for the Vaisala (BL-Index) and Lufft (Q-Index – in brackets) ceilometers, and the (bottom) percent of clear skies (no clouds measured), cloudy skies (any number and/or height of clouds measured), and missing data (e.g., instrument failure, etc.) at each site. The values in parentheses indicate the percent of sky conditions below 7600 m in order to directly compare the ceilometers.

Ceilometer Data	US-Ho1 2013 – 2019	US-KFS 2016 – 2019	US-ARM 2012 – 2020	US-Wkg/Whs 2017 – 2020
BL Index 1	27.3%	13.5%	14.7%	2.2% [5-6]
BL Index 2	44.8%	41.2%	45.1%	59.6% [3-4]
BL Index 3	27.9%	45.3%	40.2%	38.2% [1-2]
Clear	47.4%	51.9% (59.3%)	64.2%	60.5% (68.5%)
Cloudy	52.6%	48.1% (40.7%)	35.8%	39.5% (31.5%)
Missing	24.0%	13.5%	1.2%	23.9%

3.2. Characteristics of clouds and MLH

The second objective was to analyze the seasonal patterns of clouds and MLH across different ecosystems. Clouds were present year-round at all the sites, but the frequency of cloud cover was dependent on the site location (Table 2). US-Ho1 had the highest frequency of clouds (52.6%) across all sites. When only considering the lowest 7600 m of the atmosphere (a uniform height across all ceilometers), the sky conditions at the remaining sites essentially followed the national aridity gradient (Table 1). There was a decrease in cloud cover from US-Ho1 to US-KFS (40.7%), a further decrease found at US-ARM (35.8%), and lastly US-Wkg/Whs (31.5%), a result of decreasing water supply to feed cloud formation (Table 2).

The monthly mean MLH was then analyzed at each site (Fig. 4). At US-Ho1, the monthly mean MLH was the most variable in spring, coinciding with the timing of snowmelt and the start of the forest's growing season, while the highest ceilometer heights were found in late summer (Fig. 4a). At US-KFS (Fig. 4b), the highest monthly mean values were shown to occur in late spring (April) before steadily decreasing for the remainder of the year. The monthly mean MLH at US-ARM followed a clear seasonal pattern, with the lowest values in the winter and the highest mean values (1600 m) during the summer (Fig. 4c). There was little year-to-year variation in the monthly mean ceilometer-derived MLH at US-Wkg/Whs (Fig. 4d) outside of the late-summer months (August and September). However, there was a pronounced seasonal pattern (similar to that of US-ARM) and summer maximum (2700 m) when using the STRATfinder method. These monthly heights, the highest of all the sites, peaked during the driest and hottest months, with more variability during the summer rainy season.

US-Ho1 was the only site that had NARR monthly PBLH lower than ceilometer MLH but was within the range of ceilometer values measured. The spring and summer NARR data at US-KFS suggests an overestimation of MLH when compared to ceilometer MLH but yields similar values in other seasons. Lastly, there was good agreement between the datasets at US-ARM and US-Wkg/Whs (STRATfinder method only), where the mean monthly ceilometer MLH were nearly identical in shape, yet considerably lower in magnitude than the mean NARR PBLH.

With the site-specific cloud frequencies and monthly MLH identified, we then assessed the variability in the diurnal growth and evolution of

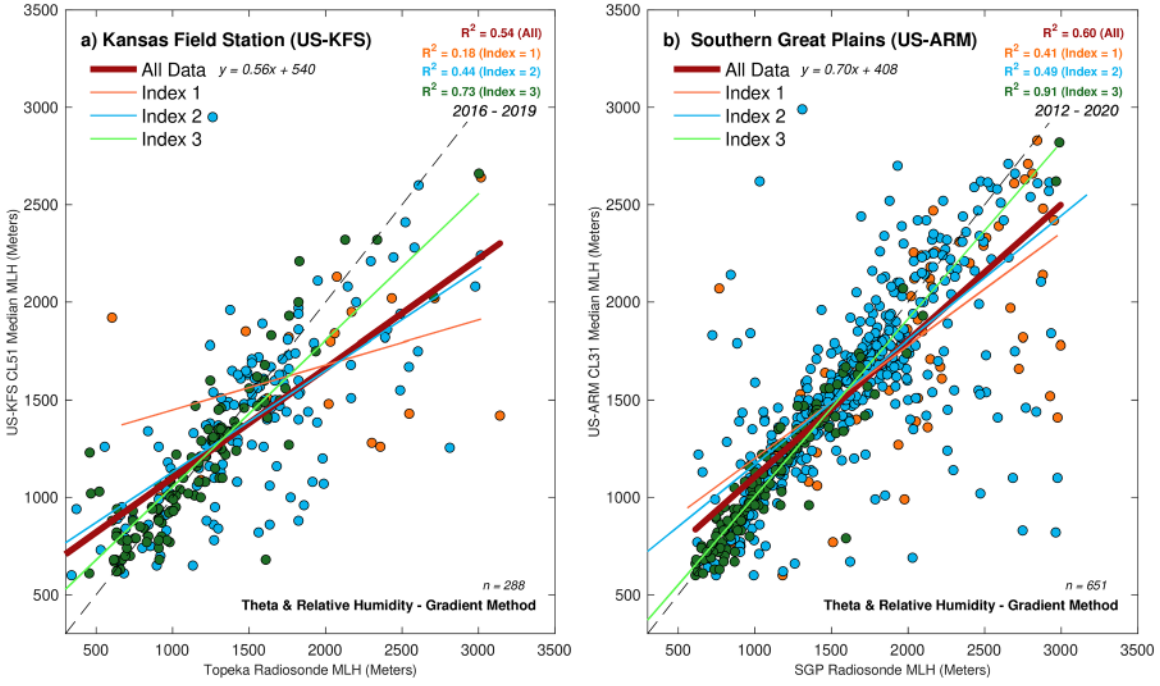

Fig. 3. Relationships between the gradient method derived radiosonde MLH and ceilometer MLH at (a) Kansas Field Station (US-KFS), and (b) Southern Great Plains (US-ARM). Points were sorted by ceilometer quality index, with solid lines illustrating the fit of each dataset.

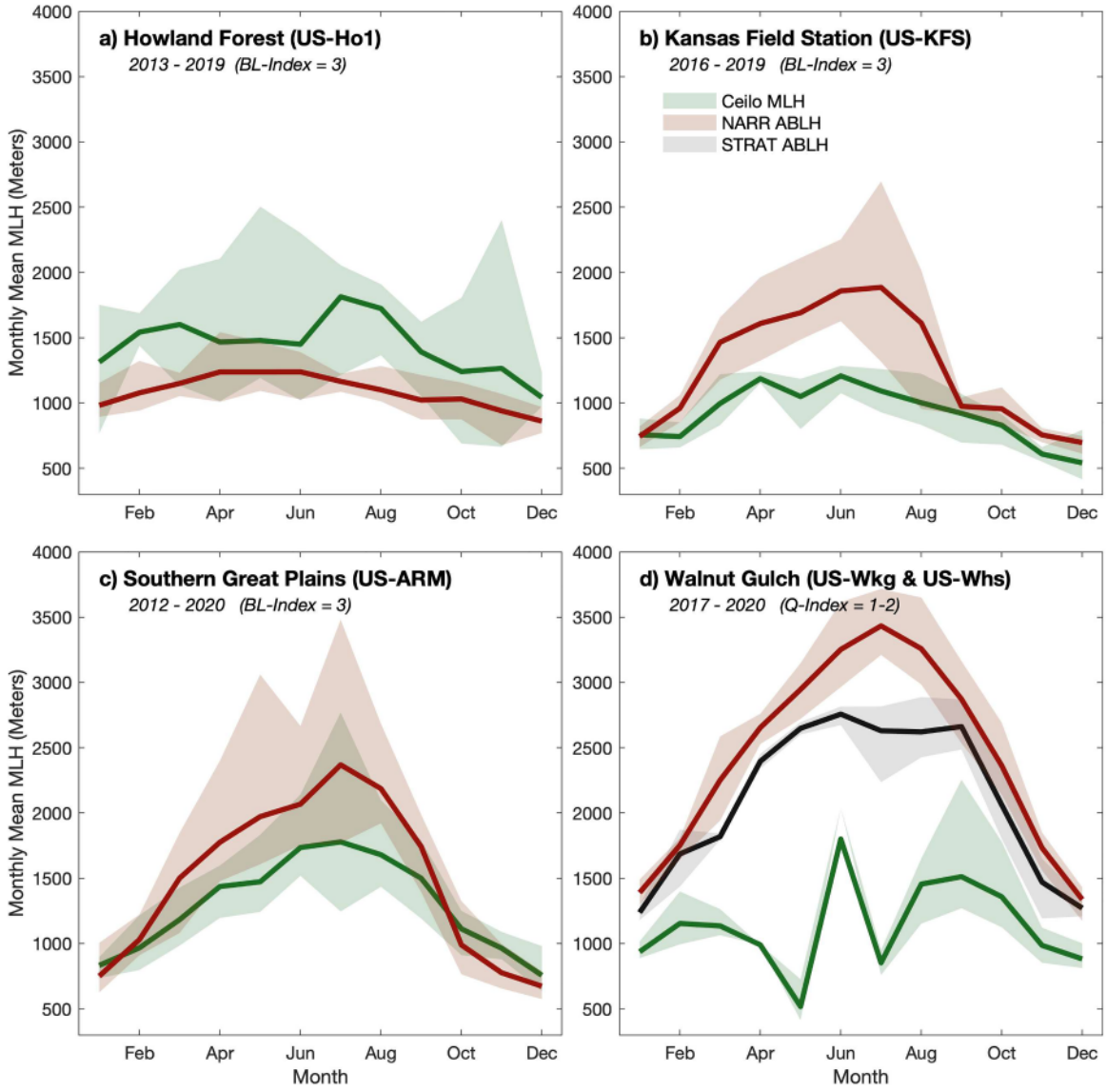

Fig. 4. Mean monthly ceilometer (Ceilo; green), NARR (red), and STRATfinder (STRAT; gray) afternoon median MLH at (a) Howland Forest (US-Ho1), (b) Kansas Field Station (US-KFS), (c) Southern Great Plains (US-ARM), and (d) the WGEW sites (US-Wkg & US-Whs). Color shading represents the min and max monthly MLH during the period of measurements.

MLH that resulted from clear and cloudy sky conditions and therefore different surface forcings (Fig. 5). Using data from all-seasons, half-hourly ensemble averages were compiled. The largest difference was found at US-Ho1, with MLH under clear sky conditions ~600 m higher than the MLH during cloudy conditions. During these clear periods, the MLH rapidly deepened after sunrise, before reaching an average height close to 1600 m in the late afternoon. A slower developing and shallower (~1000 m) MLH was measured when clouds were present at US-Ho1. The daily development of MLH at US-KFS and US-ARM followed similar patterns when separated by sky condition, varying between 400 m and 600 m at each site in the late afternoon. These general characteristics (growth after sunrise and higher MLH under clear skies) were also found by the ceilometer at US-Wkg/Whs, but to a lesser extent when using the STRATfinder method (Fig. 5d). Ultimately, the differences in MLH as a result of varying sky conditions were likely attributable to the differences in surface forcing variables under similar conditions (Fig. 6). At each site, the magnitudes of clear and cloudy MLH closely resembled the magnitudes of H. Moreover, under clear skies, T_{diff} was more negative (warmer surface temperatures), and VPD, LE, and H were higher when compared to cloudy skies, which served to promote increasing growth in daytime ensemble MLH values.

In all cases, the ensemble mean MLH was found to be higher under clear skies and followed a well-defined evolution of diurnal growth, depicted by shallow stable conditions overnight and in the early mornings, before rapidly deepening with increasing solar radiation during the day. Next, the diurnal evolution of the ensemble mean MLH, separated by season and for all sky conditions, was examined (Fig. 7). As expected, the MLH at all locations was the lowest in winter, when lower net radiation and shorter days act to suppress the growth of the mixing layer. The mean MLH during shoulder seasons (spring and autumn) were nearly identical to one another at every site (green and orange lines) and were often similar in height to the mean annual MLH. There was significant variability in the seasonal MLH at US-Ho1, the site with the lowest amount of high-quality data (Table 2). At US-KFS, as suggested in Fig. 4, MLH in the spring were some of the highest all year, even rivaling MLH at that site during summer (Fig. 7b). The MLH reached their maximum values at all sites during the summer months due to increased net radiation, warmer temperatures, and a likely increase in the sensible heat flux. The largest winter to summer seasonal difference in ensemble MLH was measured at US-ARM (~900 m) and at US-Wkg/Whs (> 1000

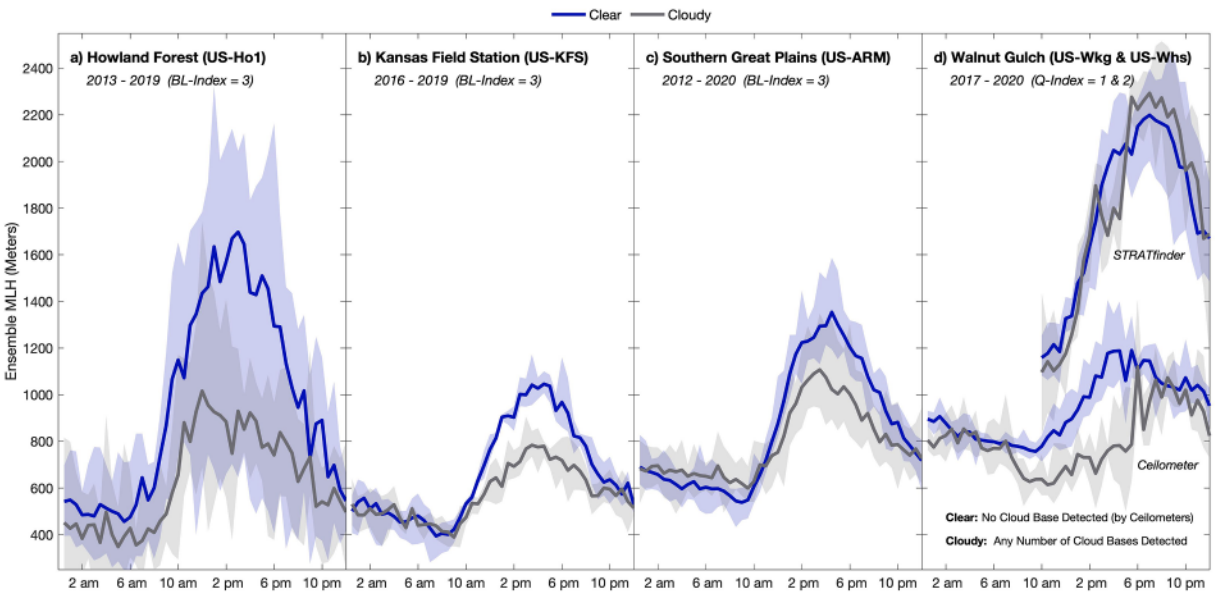

Fig. 5. Half-hourly ensemble average ceilometer data illustrating the diurnal evolution of MLH for clear (blue) and cloudy (grey) conditions, with blue and grey shading representing the minimum and maximum range of half-hourly MLH at the four sites (a – d same as Fig. 4).

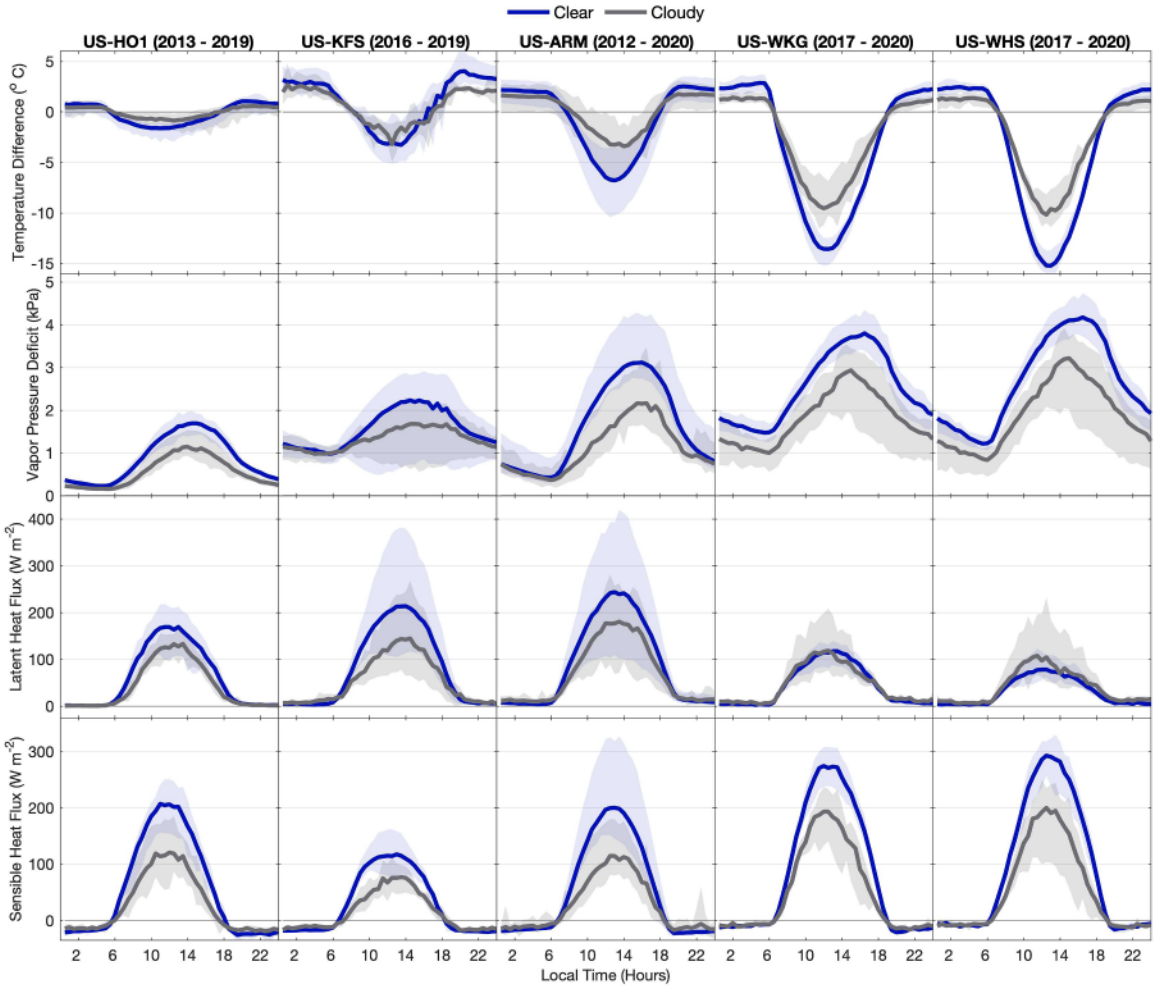

Fig. 6. Half-hourly ensemble average data highlighting the diurnal evolution of energy and meteorological fluxes for clear and cloudy conditions (same as Fig. 5).

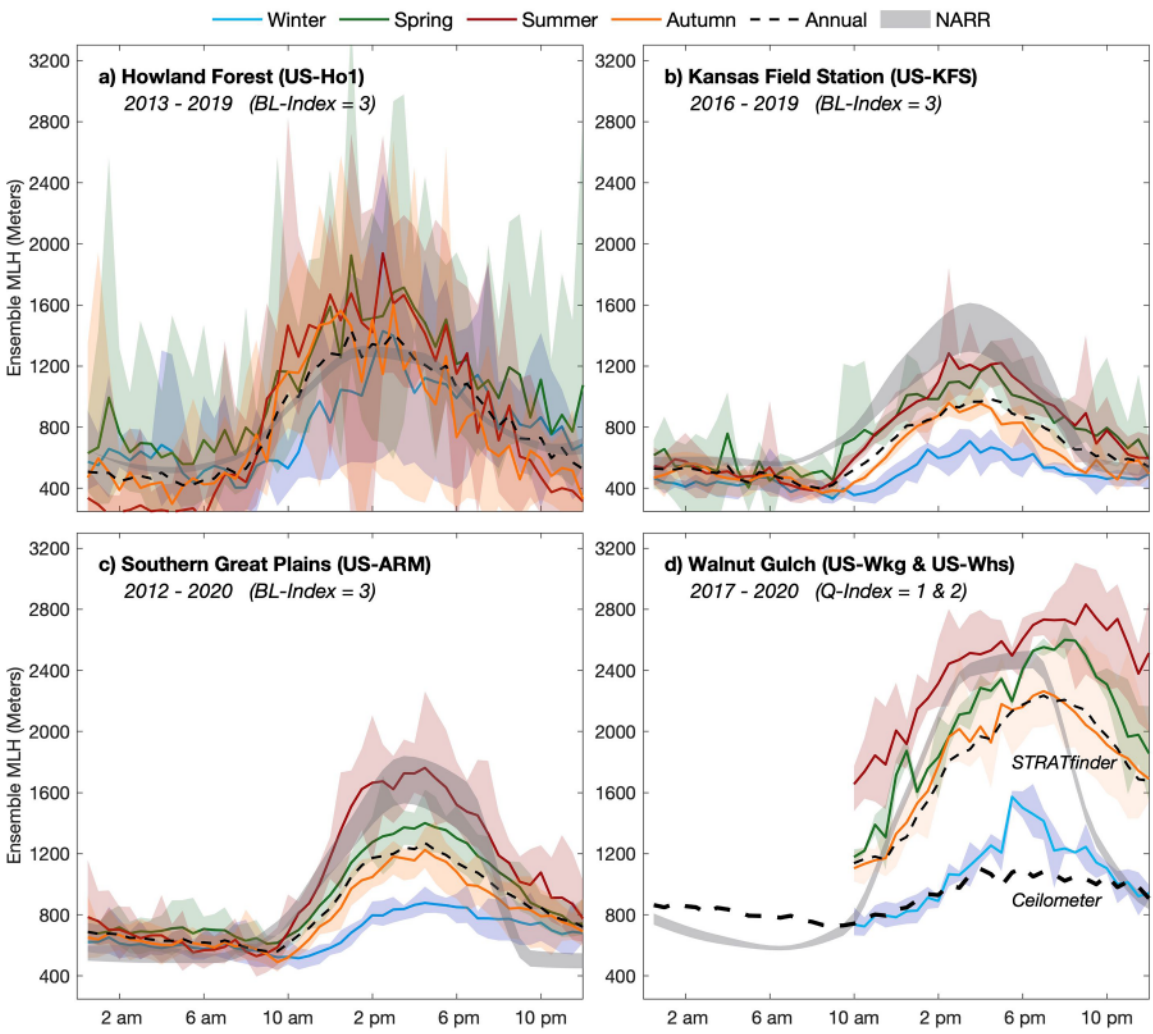

Fig. 7. Half-hourly ensemble MLH separated by season (e.g., winter, spring, summer, autumn, and annual) at the four ceilometer sites. The shading is the same as previously described, with the annual ensemble NARR PBLH data (grey) also included.

m) when using the STRATfinder method.

These data were then compared against the ensemble mean NARR PBLH data in order to estimate if the heights found at each site were within the range one might expect. At US-Ho1, the mean ensemble NARR data essentially traced the mean ceilometer MLH data (dashed line). The NARR PBLH were also similar to the ceilometer MLH at US-KFS and US-ARM, albeit slightly higher than the mean ceilometer values. However, the NARR PBLH data was able to effectively capture the timing and general growth of the ensemble MLH at both of those sites. Lastly, at US-Wkg/Whs, the NARR PBLH data were comparable in magnitude to the estimated MLH from the STRATfinder method, although the STRATfinder method produced peak ensemble values later in the day, which may be an artifact of the method calculations (possibly capturing the residual layer). Lastly, NARR PBLH data at those sites were nearly double the height of the ceilometer MLH (thick dashed line), highlighting the issues previously outlined.

3.3. Role of surface processes on MLH

Following the monthly mean and ensemble MLH patterns at each site, we analyzed the role of seasonal surface fluxes, phenology, and environmental factors on MLH dynamics. We examined the relationships between the bin-averaged (or weighted moving average) responses of explanatory variables and the median late-afternoon ceilometer MLH (Fig. 8). At all sites, an increase in H led to an increase in MLH. To differing degrees, an increase in bin-averaged LE led to a slight increase in MLH at each of the sites. At all the sites, VPD was the most strongly correlated with increasing MLH. While the levels of VPD varied between sites, being much lower at US-Ho1 compared to US-ARM and US-Wkg/Whs, all sites illustrated a nearly 1000 m average increase in MLH with a 2 kPa increase in VPD. The MLH decreased with an increase (positive values) in T_{diff}. This effect was the most pronounced at US-Wkg/Whs and was effectively nonexistent at US-Ho1. At US-ARM and US-Wkg/Whs, warmer surface temperatures and increasing differential surface heating (negative T_{diff}) acted to promote the growth of the MLH, but if T_a was warmer than T_{sfc}, typical of a stable inversion layer or wet periods (or during periods of negative H), very shallow MLH were observed at those sites. Apart from increasing MLH with increasing greenness (PhenoCam Gcc) at US-KFS and slightly at US-Ho1, bin-averaged volumetric soil water content (θ_{10cm}), Gcc, and HI_{Low} had little impact on modifying MLH at all sites. For these variables, the bin-averaged MLH was relatively constant across their measured ranges for all years of measurements.

3.4. Relative influence of explanatory variables

The final objective of the study was to examine the relative influence of explanatory variables on MLH at each site. We ran seasonal and annual boosted regression trees (BRT) to further determine the relative strength or association of those same seven sub-surface (θ_{10cm}), surface

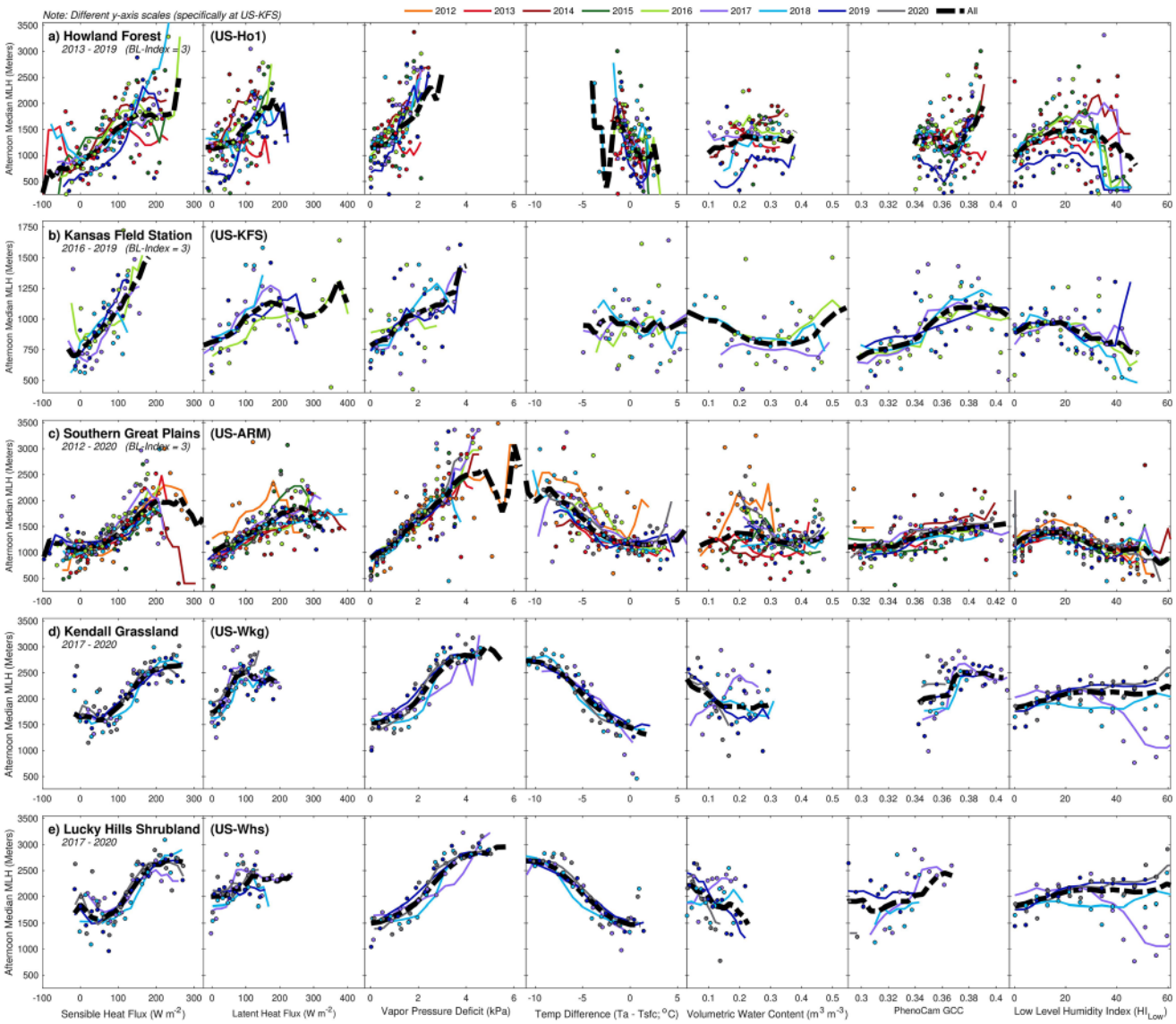

Fig. 8. Bin-averaged sensible heat flux (H, site-specific bin size of 12.5 – 15 Wm^{-2}), latent heat flux (LE, 12.5 – 25 Wm^{-2}), vapor pressure deficit (VPD, 0.15 – 0.25 kPa), air and surface temperature difference (T_{diff}, 0.25 – 0.75°C), volumetric soil water content (θ_{10cm}, 0.2 – 0.35 m^3 m^{-3}), PhenoCam Gcc (Gcc, 0.003 – 0.0075 Gcc), and the low-level humidity index (HI_{Low}, 2.5 – 3°C) for all sites. Dashed black lines are the moving averages across all years of measurements.

(LE, H, VPD, and Gcc), and atmospheric stability (T_{diff} and HI_{Low}) explanatory variables on afternoon median ceilometer MLH (Fig. 9). During the winter, when MLH was the lowest of any season, the relative influence of explanatory variables on MLH was revealed to be sporadic, with slight associations due to heat fluxes at US-Ho1 and US-ARM, Gcc at US-KFS, and T_{diff} at US-Wkg/Whs. In spring, H and LE had the most impact on MLH at US-Ho1 and US-KFS, VPD at US-ARM, θ_{10cm} at US-Wkg, and Gcc at US-Whs. The winter and spring data at each site had the lowest BRT model performance (R^2) and fewer total data points than the other seasons (Fig. 10; Table 3). At US-Ho1 and US-KFS, similar erratic associations were evident in all remaining seasons and when considering all of the data, with an overall slight relative strength in determining annual MLH resulting from H at US-Ho1 and LE at US-KFS. However, these sites had the lowest BRT model performance (Fig. 9; Table 3).

At US-ARM, the seasonal results were much more consistent, with MLH associated with VPD at all times (~40% of influence), with secondary forcings as a result of heat fluxes (LE and H). Autumn was the season with the highest BRT performance at US-ARM (R^2 = 0.54). During this season, there was a significant positive relationship between ceilometer MLH and BRT MLH, even able to explain large deviations (from 500 m to 2500 m) in ceilometer MLH (Fig. 10). Ultimately, the impacts of VPD on MLH shaped the entire dataset ('annual'), with the relative strength of the remaining explanatory variables providing a trivial (< 10%) impact on ceilometer MLH.

The MLH data using the STRATfinder method at US-Wkg/Whs produced some of the highest seasonal BRT relationships (R^2 > 0.50). In summer, surface temperature and humidity appeared to have the largest impact on the sites, with T_{diff} (VPD) most largely impacting MLH at US-Wkg (US-Whs). In the autumn, the seasonal grassland at US-Wkg was most associated with changes in Gcc, while the US-Whs surface data was most associated with T_{diff}. At both sites, T_{diff} was the dominant influence across all seasons (when considering all the data) with secondary associations from VPD. This relative strength due to differential surface heating (and thus H) was highlighted previously, as these two sites saw the largest difference between T_{sfc} and T_a and the highest H (Fig. 6). Lastly, the flux data at US-Wkg/Whs produced the highest annual BRT R^2 (0.65), effectively capturing the deviations in STRATfinder MLH (Fig. 10).

The analysis up to this point included data from all sky conditions,

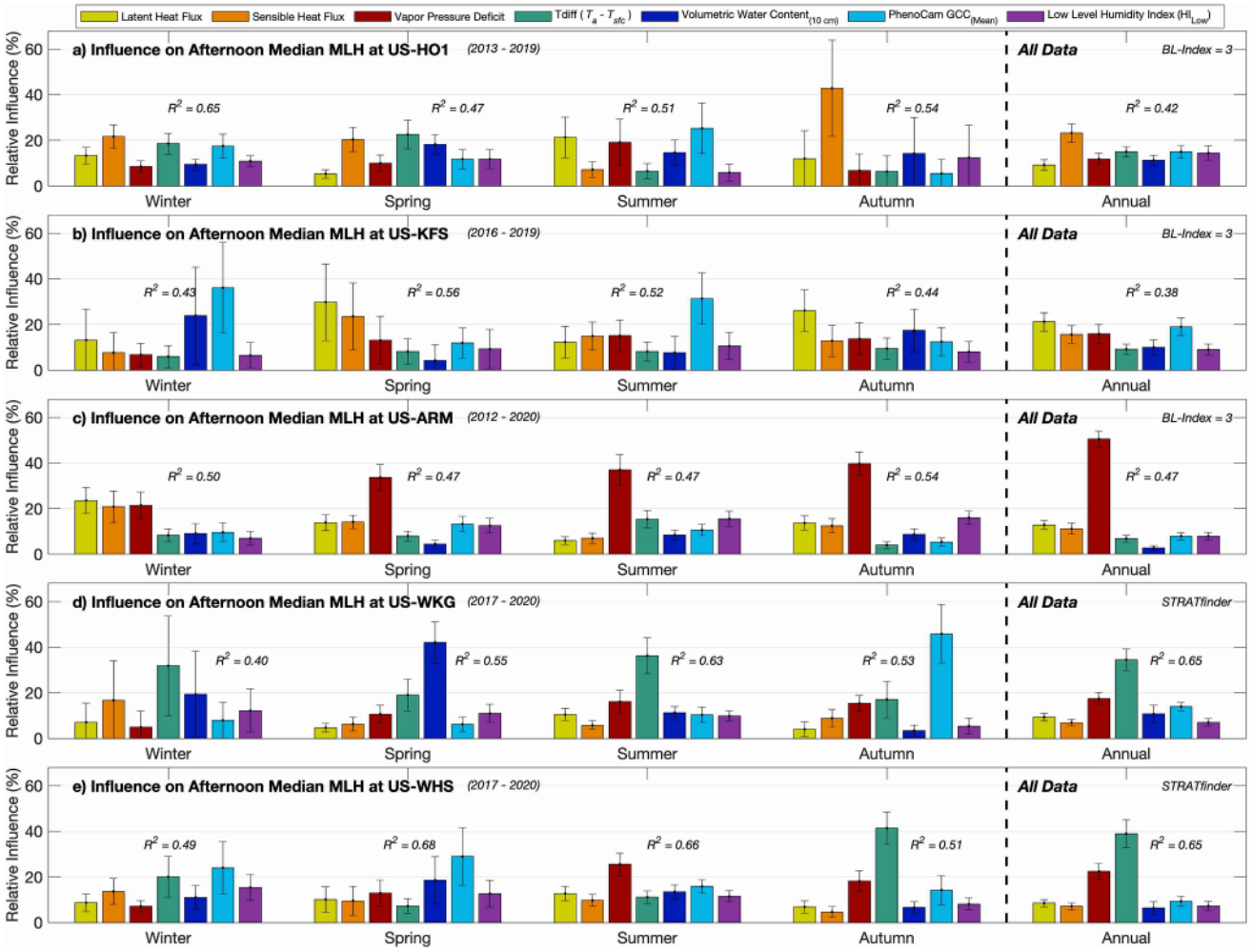

Fig. 9. Bar plots of the seasonal and annual boosted regression tree (BRT) relative influences of explanatory variables on ceilometer (or STRATfinder) median MLH for the five sites with error bars and model performance (R^2). The explanatory variables and sites are the same as those listed in Fig. 8.

but in order to be relevant to basic ABL models and attempt to capture unobstructed MLH growth (without the present of clouds, fog, rain, etc.), we also evaluated the same ceilometer MLH using only data under clear-sky conditions (Fig. S2). Increases in model performance were found at each site for all seasons except for summer when convective processes often dominate. While only few clear-sky days were detected at US-Ho1 (Table 2), the BRT MLH output improved significantly, resulting in an increased ability to model ceilometer MLH. US-KFS and US-ARM were similar to before, with slight improvements when considering all data. Lastly, the US-Wkg/Whs 'annual' relationships were the highest of any of the sites (R^2 = 0.70-0.76), suggesting that the surface flux data were able to accurately capture changes in the STRATfinder data at those sites.

4. Discussion

This study examined long-term co-located surface flux and ceilometer data from five AmeriFlux sites that spanned extensive climatological (temperature and precipitation) and ecosystem (plant functional type) gradients to better understand the seasonal roles of surface fluxes on the height of the mixing layer (MLH). We used monthly, seasonal, ensemble, and bin averages of half-hourly and daily datasets to examine the variability and evolution of MLH under various meteorological forcings, and we incorporated a boosted regression tree (BRT) analysis into this study to model the relative influences of explanatory variables on seasonal changes in MLH. We found evidence that eddy covariance flux tower-based measurements of sensible (H) and latent (LE) heat fluxes, vapor pressure deficit (VPD), and the difference (T_{diff}) between the surface temperature (T_{sfc}) and air temperature (T_a) were most strongly associated with daily MLH. These influences varied among the ecosystems but were relatively consistent for the sites with the highest seasonal correlations between observed and predicted MLH, namely US-ARM and US-Wkg/Whs. This discussion highlights the causes for the overall variability in MLH observed at each site and considers the continued importance of incorporating surface flux measurements into future MLH studies.

4.1. Ancillary atmospheric observations

We began the analysis by examining the relationships between radiosonde MLH and ceilometer MLH at two sites: US-KFS and US-ARM. Previous studies have shown significant agreement between the MLH estimated using both of these data sources (Martucci et al., 2007; Münkel et al., 2007). We therefore included the radiosonde MLH as a reference to determine the general credibility of the ceilometer MLH used throughout this analysis, as suggested in previous studies (Kotthaus and Grimmond, 2018; Tang et al., 2016). We found a positive correlation between the two datasets at US-KFS, although it is possible that the distance between the two measurements (roughly 30 km) impacted this relationship. While we expect the MLH to be relatively stable over large areas, spatial differences in H due to changes in soil moisture, land-use, or complex terrain influence MLH (Bianco et al.,

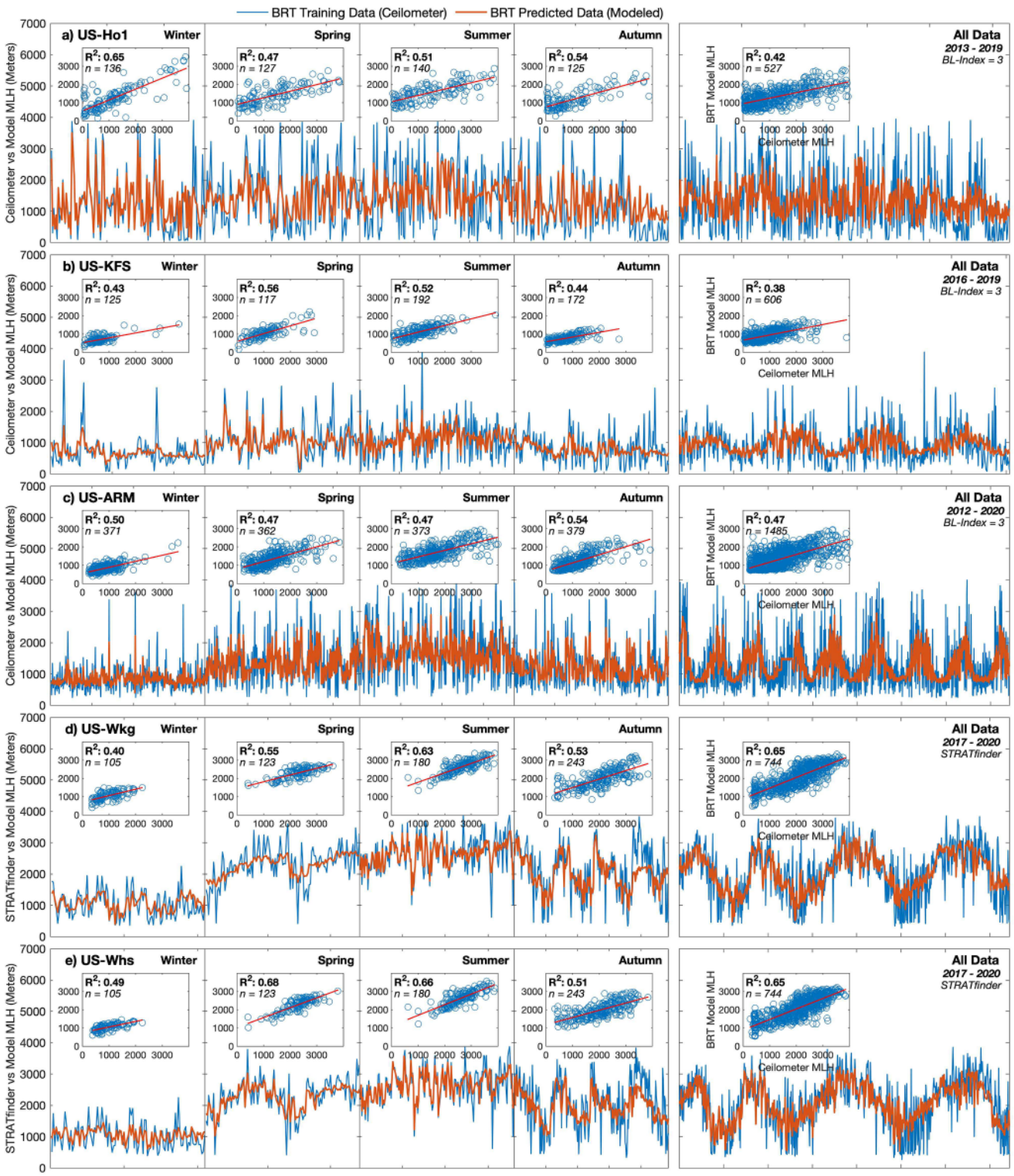

Fig. 10. Seasonal and total line plots of the relationships between the ceilometer (training) and STRATfinder MLH data (both blue) and the BRT model output MLH (orange) for each site. Scatter plots of the data are shown in each Fig. inset with R^2 and number of data points (n) included.

2011; Lee et al., 2013; Lee and De Wekker, 2016). For that reason, most studies often consider co-located measurements, which were available at US-ARM. The most significant and strongest positive relationships were found at US-ARM when using the highest quality ceilometer data, likely representative of when a clear aerosol boundary and well-defined MLH were present (Münkel et al., 2007). We realize that ambiguous MLH estimations may occur under non-ideal conditions (Collaud Coen et al., 2014; Salcido et al., 2020) or due to varying surface or spatial differences (like at US-KFS), and since we did not separate the data based on meteorological conditions or atmospheric stability, we were satisfied with the results, especially since they were comparable to that of similar studies (e.g., Chandra et al., 2010).

We also examined the frequency and impact of clouds on regulating the land-atmosphere exchange of energy. Our findings on cloud

Table 3
The seasonal and total linear relationships (R^2 in bold) between ceilometer median MLH (input) and modeled boosted regression tree (BRT) MLH (output), and the total number of daily data points used for each BRT model run (in parentheses) at the five AmeriFlux sites.

All Skies	Winter	Spring	Summer	Autumn	All Data
US-Ho1	**0.65** *(n 136)*	**0.47** *(n 127)*	**0.51** *(n 140)*	**0.54** *(n 125)*	**0.42** *(n 527)*
US-KFS	**0.43** *(n 125)*	**0.56** *(n 117)*	**0.52** *(n 192)*	**0.44** *(n 172)*	**0.38** *(n 606)*
US-ARM	**0.50** *(n 371)*	**0.47** *(n 362)*	**0.47** *(n 373)*	**0.54** *(n 379)*	**0.47** *(n 1485)*
US-Wkg	**0.40** *(n 105)*	**0.55** *(n 123)*	**0.63** *(n 180)*	**0.53** *(n 243)*	**0.65** *(n 744)*
US-Whs	**0.49** *(n 105)*	**0.68** *(n 123)*	**0.66** *(n 180)*	**0.51** *(n 243)*	**0.65** *(n 744)*
Clear Skies	**Winter**	**Spring**	**Summer**	**Autumn**	**All Data**
US-Ho1	**0.71** *(n 29)*	**0.67** *(n 22)*	**0.64** *(n 34)*	**0.90** *(n 39)*	**0.67** *(n 124)*
US-KFS	**0.62** *(n 29)*	**0.75** *(n 25)*	**0.55** *(n 81)*	**0.58** *(n 68)*	**0.54** *(n 204)*
US-ARM	**0.52** *(n 165)*	**0.65** *(n 117)*	**0.50** *(n 176)*	**0.56** *(n 188)*	**0.53** *(n 646)*
US-Wkg	**0.46** *(n 90)*	**0.55** *(n 68)*	**0.62** *(n 70)*	**0.72** *(n 143)*	**0.70** *(n 371)*
US-Whs	**0.62** *(n 90)*	**0.57** *(n 68)*	**0.66** *(n 70)*	**0.71** *(n 143)*	**0.76** *(n 371)*

frequencies were consistent with An et al., (2017) who found the highest annual cloud cover to typically be in the northeastern US (45%), slightly lower cloud cover in the central US (39%), and the lowest cloud cover in the southwestern US (27%). Cloud amounts (and types) influence the growth of the MLH (Kotthaus and Grimmond, 2018), so we assessed the impacts of cloud coverage on MLH at each site. Pal et al., (2013) suggested that separating MLH regimes by cloud cover identifies days dominated by surface-driven buoyancy (clear) and those driven by larger-scale effects (cloudy). By using this general method, we found the daytime MLH at each site to be consistently higher under clear skies (larger T_{diff} and larger H) as opposed to cloudy skies, as suggested by (Ramanathan et al., 1989).

4.2. Temporal patterns of MLH

Our analysis revealed that the evolution and magnitude of the mean monthly MLH were substantially different across the sites. The highest winter and spring mean monthly MLH across all sites was found at US-Ho1 (Fig. 4). While US-Ho1 was the only forest examined within this study, this finding was consistent with past studies that observed deeper MLH over forests (when compared to shorter vegetation), due to higher H and surface roughness (Baldocchi and Ma, 2013; Barr and Betts, 1997; Li et al., 2021). Additionally, the relatively higher MLH in the winter at US-Ho1 was likely due to the forest darkening the typically snow-covered land surface (decreasing albedo), warming the surrounding air, and effectively building the MLH (Lee et al., 2011; Sellers et al., 1997). For shorter vegetation, like the croplands, grasslands, and shrublands at the other sites, we saw lower mean monthly MLH during this period, but higher MLH during the summer. US-KFS saw maximum monthly MLH between April and June, likely due to the greenup (phenology) of the native grasses at that site, where the maximum H occurred prior to full leaf-out (Yi et al., 2001). The results from US-ARM were consistent with past studies, where we saw the highest mean monthly MLH in the early part of the summer (e.g., June) when soils at each site were the driest, which resulted in decreased LE and increased H relative to wetter soil conditions (Desai et al., 2006; Schmid and Niyogi, 2012). Lastly, there was not much variability in mean monthly MLH at US-Wkg/Whs except during the summer months, which coincided with the variable presence of the North American Monsoon (Higgins et al., 1997). Even so, the summer mean ceilometer MLH at US-Wkg/Whs was roughly 500 m 1000 m lower than similar studies (and NARR data) in the area. Instead, the STRATfinder data followed the same seasonal pattern with moderately higher mean MLH than outlined in previous studies of the area (Perkins, 2020; Sanchez-Mejia and Papuga, 2014; Sorooshian et al., 2011).

The MLH also depends on the season, time of day, and local conditions (de Haij et al., 2007) so we examined the seasonal ensemble patterns of MLH at each site. The MLH slowly decreased after midnight at all sites, signifying the dissipation of a possible residual layer or other more stable atmospheric conditions (Banta et al., 2007; Caicedo et al., 2020). Prior to sunrise, a minimum in MLH was present, before increasing solar radiation helped build the MLH throughout the day (to a seasonally varying extent). At all sites, the maximum ensemble MLH was found between 3 7 pm local time, consistent with past studies (Seidel et al., 2012). The key difference between the sites was the diurnal evolution of MLH measured at US-Wkg/Whs. The ceilometer at that site often failed to capture the evolution of daytime changes in MLH, which was the reasoning for implementing the STRATfinder data. Often, there was no MLH detected during the day by the Lufft CHM15k at that site, while STRATfinder actively traced the backscatter profile to provide a real estimate that was otherwise unaccounted for by the ceilometer (Fig. S1). It is possible that the low aerosol loadings and typical clear skies in the southernmost deserts of Arizona led to rather unreliable MLH retrievals. A drawback with a variety of ceilometers has long been their general inability to detect MLH under clean air (low molecular scattering) or if the ceilometer signal-to-noise ratio is too low (Eresmaa et al., 2006; Kotthaus and Grimmond, 2018; Wiegner et al., 2014). We also had difficulty measuring the MLH with another co-located ceilometer that was installed at that site, a Campbell Scientific CS135. Like the Lufft CHM15k but worse, the CS135 was unable to resolve any patterns in MLH (Fig. S1), pointing to the challenge of making such measurements in the arid high-desert environment. However, this may be an opportunity for extreme tests of ceilometer instrument performance in locations such as this and may make it an appropriate area for future studies.

4.3. Controls of surface fluxes on MLH

The MLH and its properties are driven by the bi-directional thermal and dynamic effects of the atmosphere and the land surface (Beamesderfer et al., 2022; Zilitinkevich et al., 2012). Recent studies have identified the important linkages between local and regional land surface and atmospheric variables on the growth and evolution of the MLH (Baldocchi and Ma, 2013; Betts and Silva Dias, 2010; Santanello et al., 2007; Yi et al., 2004). This study similarly looked to identify the key surface controls that were associated with changes in daily MLH. We found tower flux-based measurements of H, LE, VPD, and T_{diff} to have the largest impacts on MLH at our study sites. At all sites, a bin-averaged increase (decrease) in H, LE, or VPD (T_{diff}) resulted in an increase in MLH. It is known that the primary driving factor of MLH is H, with increased surface heating leading to increased MLH growth (Santanello et al., 2005; Yi et al., 2001). We also saw slight increases in bin-averaged MLH with increasing LE, a result of the buoyant effects of heat fluxes and the surface impacts of net radiation (and effectively H), as evaporation (LE) is strongly tied to net radiation (Baldocchi and Ma, 2013; Koster et al., 2009; Vick et al., 2016). The bi-directional effects of humidity and temperature on MLH within the mixing layer were emphasized by daily fluctuations in VPD. Whether we consider changes in temperature and/or humidity to result from the effects of dry-air entrainment feedback (Konings et al., 2010; Santanello et al., 2007) or from stomata

closing (lowering LE) in response to high VPD (Lansu et al., 2020), all sites saw a pronounced and consistent increase in MLH with increasing VPD (and VPD increasing as a result of increasing MLH).

The remaining variables appeared to have a lesser importance in terms of their association to MLH at all sites. To a varying degree (excluding US-KFS), there was an increase (reduction) in MLH with decreasing (increasing) T_{diff}. This difference between T_a and T_{sfc} is known to be driven by both land surface properties and atmospheric interactions (e.g., clouds) (Jin and Dickinson, 2010). In this case, cooler or more stable conditions suppress the MLH, while differential surface heating and higher H (negative T_{diff}) would lead to higher MLH (Betts, 2000; Panwar et al., 2019). We saw little variation in bin-averaged MLH as a result near-surface soil water content ($_{10cm}$). Such relationships have been previously examined in great detail and reflect the broader impacts of wet and dry soils on MLH that result from changes in H, LE, or VPD (Konings et al., 2010; Koster et al., 2009; Sanchez-Mejia and Papuga, 2014; Santanello et al., 2005). The PhenoCam Gcc was only shown to have meaningful covariance on MLH at US-Ho1 and US- KFS, where Gcc parallels the seasonality of photosynthesis from the forests and native grasses (and thus LE and H) and may act as a rough indicator to predict changes in MLH resulting from land-surface phenology (Freedman et al., 2001; Yi et al., 2004). The overall stability structure of the lower atmosphere has been shown to be very important in influencing MLH (Santanello et al., 2005), yet in this study the indirect effect of the low-level humidity index (HI_{Low}) failed to capture any identifiable mean changes in MLH.

4.4. Modeling daily MLH with flux data

We used boosted regression trees (BRTs) to examine the interactive relationships between the variables that act to influence the growth of the MLH. This approach was chosen over others (e.g., univariate correlation analysis) as BRTs are able to fit complex nonlinear relationships and incorporate interaction effects between explanatory variables (Elith et al., 2008). The total (‘annual) associations of H, LE, VPD, and T_{diff} on MLH were again largely apparent. At US-Ho1, winter had the highest BRT model performance (R^2) of any season, when seasonal (winter--spring transition) increases in H rapidly warm the mixing layer (Freedman et al., 2001). In summer at US-Ho1 and autumn at US-KFS, the relative strength of LE on MLH was the highest, highlighting the seasonal impacts due to LE (and Rn) during those times (Fig. 4; Baldocchi and Ma, 2013; Salvucci and Gentine, 2013). The association between VPD and MLH at US-ARM and T_{diff} at US-Wkg/Whs stress the continued importance (e.g., mixed layer model) and coupled behavior of the air temperature and humidity relationships that exist between the surface and the MLH (Betts, 2000; Santanello et al., 2007). We also examined clear sky data to better understand the transition between cloudy MLH and clear MLH. This has important implications on MLH dynamics, as cloud development and precipitation will lead to deviations from the MLH behaviors previously addressed (Findell and Eltahir, 2003; van Stratum et al., 2014). The annual clear sky BRT correlations increased at all sites. For clear skies, large-scale evaporative (LE) processes are negligible (sufficient vertical turbulent mixing) within the MLH, and the apparent influences of H and VPD on modeling MLH may increase (Panwar et al., 2019; Santanello et al., 2005). This is likely why we saw such a significant positive relationship at US-ARM and US-Wkg/Whs, where the strength of VPD on MLH was evident across all seasons.

Overall, the use of daily flux measurements generally outlined the seasonal patterns of our ceilometer-measured MLH at each site, but by using these flux data alone, we were unable to accurately capture the complex conditions driving MLH. Some studies have suggested that the scales at which the changes in MLH occur and the scales at which measurements of flux and meteorological data occur are so different that a direct comparison between the two datasets may not be entirely feasible (Gibert et al., 2007). Other studies have emphasized the importance of categorizing MLH by various soil moisture levels or atmospheric stability conditions. Wetter or drier soil regimes can have profound impacts on the influence of surface fluxes on MLH (Sanchez-Mejia and Papuga, 2014). Likewise, if an area is dominated by high pressure or larger-scale weather phenomena, it could negate the effects of the surface conditions on MLH growth (Santanello et al., 2005). In either such case, regardless of the amount of surface heating an area has, land-atmosphere conditions during prior days and nights can act to suppress the following days MLH growth. Subsidence and advection processes have also been shown to influence the expected growth in daily MLH (Pietersen et al., 2015; Rey-Sanchez et al., 2021; Sinclair et al., 2010). Consequently, our empirical approach was unable to account for these larger-scale influences, but we anticipate a study with data separated by soil or stability conditions may have better explanatory power on MLH than the data inputs that we used.

5. Conclusions

Our study used radiosonde, reanalysis, eddy covariance, and phenological data from select AmeriFlux sites across the United States in an attempt to identify the daily and seasonal trends in ceilometer cloud frequencies and mixing layer heights (MLH) and examine the relative strength of explanatory surface variables in determining MLH. We found significant agreement between radiosonde MLH and the highest-quality ceilometer MLH retrievals at two sites (US-KFS and US-ARM) with nearby measurements. At another site (US-Wkg/Whs), the ceilometer MLH retrievals were found to be unreliable, as they did not agree with reanalysis data or other published studies. We utilized an algorithm (STRATfinder) to estimate MLH from ceilometer data at that site to more accurately estimate local MLH. The STRATfinder results provide insight on the potential use of such an algorithm for more consistent MLH retrievals from ceilometers. Overall, cloud coverage was shown to impact the growth and depth of MLH, which varied strongly across the climatic gradient of the study. Eddy covariance (single-point) tower fluxes of sensible heat flux (H), latent heat flux (LE), vapor pressure deficit (VPD), and the difference (T_{diff}) between air and surface temperatures were shown to have the largest direct and indirect relative influences on daily and seasonal MLH. However, when modeled with boosted regression trees (BRTs), the near-surface data often failed to capture the variations in MLH as captured by the ceilometers. Ultimately, the ceilometers at each site were shown to provide useful estimates of MLH but healthy skepticism and validation against independent MLH data is necessary for future studies. A key advantage to ceilometers is that they provide continuous MLH estimates unlike the labor-intensive radiosonde launches. Paired with single-point observations, we present an example on how to investigate the key land surface variables involved in the bi-directional land-atmosphere interactions, and how those complicated interactions vary across ecosystems.

Declaration of Competing Interest

The authors declare the following financial interests/personal relationships which may be considered as potential competing interests:

The lead-author (Eric Beamesderfer) and two of the co-authors (Andrew Richardson & Manuel Helbig) served as guest editors for the special issue where this manuscript is to be published. However, the review process for this manuscript submission and its revisions were handled independently by a Chief Editor for the journal.

Data availability

Data will be made available on request.

Acknowledgements

All authors acknowledge support from the DOE AmeriFlux Network Management Project for the site-level measurements used here. ADR acknowledges support from the National Science Foundation (1702697) and the Department of Energy s Office of Science (DE-SC0017167). PCS acknowledges support from the U.S. National Science Foundation (DEB 2034997). ERB and ADR acknowledge John Smith (USDA-ARS) for his help with the WGEW ceilometer and data. ERB acknowledges Marc-Antoine Drouin (LMD) for his help running raw2l1 and STRATfinder.

Supplementary materials

Supplementary material associated with this article can be found, in the online version, at doi:10.1016/j.agrformet.2023.109687.

References

An, N., Wang, K., Zhou, C., Pinker, R.T., 2017. Observed variability of cloud frequency and cloud-base height within 3600 m above the surface over the contiguous United States. J. Clim. 30, 3725 3742. https://doi.org/10.1175/JCLI-D-16-0559.1.

Bagley, J.E., Kueppers, L.M., Billesbach, D.P., Williams, I.N., Biraud, S.C., Torn, M.S., 2017. The influence of land cover on surface energy partitioning and evaporative fraction regimes in the U.S. Southern Great Plains. J. Geophys. Res. Atmospheres 122, 5793 5807. https://doi.org/10.1002/2017JD026740.

Baldocchi, D., Falge, E., Gu, L., Olson, R., Hollinger, D., Running, S., et al., 2001. FLUXNET: a new tool to study the temporal and spatial variability of ecosystem scale carbon dioxide, water vapor, and energy flux densities. Bull. Am. Meteorol. Soc. 82, 2415 2434. https://doi.org/10.1175/1520-0477(2001)082 2415:FANTTS 2.3.CO;2.

Baldocchi, D., Ma, S., 2013. How will land use affect air temperature in the surface boundary layer? Lessons learned from a comparative study on the energy balance of an oak savanna and annual grassland in California, USA. Tellus B Chem. Phys. Meteorol. 65, 19994. https://doi.org/10.3402/tellusb.v65i0.19994.

Banta, R.M., Mahrt, L., Vickers, D., Sun, J., Balsley, B.B., Pichugina, Y.L., Williams, E.J., 2007. The very stable boundary layer on nights with weak low-level jets. J. Atmospheric Sci. 64, 3068 3090. https://doi.org/10.1175/JAS4002.1.

Barr, A.G., Betts, A.K., 1997. Radiosonde boundary layer budgets above a boreal forest. J. Geophys. Res. Atmospheres 102, 29205 29212. https://doi.org/10.1029/97JD01105.

Beamesderfer, E.R., Buechner, C., Faiola, C., Helbig, M., Sanchez-Mejia, Z.M., Yanez-Serrano, A.M., Zhang, Y., Richardson, A.D., 2022. Advancing cross-disciplinary understanding of land-atmosphere interactions. J. Geophys. Res. Biogeosciences 127. https://doi.org/10.1029/2021JG006707.

Betts, A.K., 2000. Idealized Model for Equilibrium Boundary Layer over Land. J. Hydrometeorol. 1, 507 523. https://doi.org/10.1175/1525-7541(2000)001 0507:IMFEBL 2.0.CO;2.

Betts, A.K., 2004. Understanding hydrometeorology using global models. Bull. Am. Meteorol. Soc. 85 (11), 1673 1688. https://doi.org/10.1175/BAMS-85-11-1673.

Betts, A.K., Silva Dias, M.A.F., 2010. Progress in understanding land-surface-atmosphere coupling from LBA research. J. Adv. Model. Earth Syst. 2, 6. https://doi.org/10.3894/JAMES.2010.2.6.

Bianco, L., Djalalova, I.V., King, C.W., Wilczak, J.M., 2011. Diurnal evolution and annual variability of boundary-layer height and its correlation to other meteorological variables in California s Central Valley. Bound. Layer Meteorol. 140, 491 511. https://doi.org/10.1007/s10546-011-9622-4.

Brunsell, N.A., Schymanski, S.J., Kleidon, A., 2011. Quantifying the thermodynamic entropy budget of the land surface: is this useful? Earth Syst. Dyn. 2, 87 103. https://doi.org/10.5194/esd-2-87-2011.

Butterworth, B.J., Desai, A.R., Townsend, P.A., Petty, G.W., Andresen, C.G., Bertram, T. H., et al., 2021. Connecting land atmosphere interactions to surface heterogeneity in CHEESEHEAD19. Bull. Am. Meteorol. Soc. 102 (2), E421 E445. https://doi.org/10.1175/BAMS-D-19-0346.1.

Caicedo, V., Delgado, R., Sakai, R., Knepp, T., Williams, D., Cavender, K., Lefer, B., Szykman, J., 2020. An automated common algorithm for planetary boundary layer retrievals using aerosol lidars in support of the US EPA photochemical assessment monitoring stations program. J. Atmos. Oceanic Technol. 37 (10), 1847 1864. https://doi.org/10.1175/JTECH-D-20-0050.1.

Campbell, G.S., Norman, J.M., 1998. Introduction to Environmental Biophysics, 2nd ed. Springer, New York.

Chandra, A.S., Kollias, P., Giangrande, S.E., Klein, S.A., 2010. Long-term observations of the convective boundary layer using insect radar returns at the SGP ARM climate research facility. J. Clim. 23, 5699 5714. https://doi.org/10.1175/2010JCLI3395.1.

Collaud Coen, M., Praz, C., Haefele, A., Ruffieux, D., Kaufmann, P., Calpini, B., 2014. Determination and climatology of the planetary boundary layer height above the Swiss plateau by in situ and remote sensing measurements as well as by the COSMO-2 model. Atmospheric Chem. Phys. 14, 13205 13221. https://doi.org/10.5194/acp-14-13205-2014.

de Haij, M., Wauben, W., Baltink, H.K., 2007. Continuous mixing layer height determination using the LD-40 ceilometer: a feasibility study, De Bilt: Royal Netherlands Meteorological Institute (KNMI).

De ath, G., 2007. Boosted trees for ecological modeling and prediction. Ecology 88, 243 251. https://doi.org/10.1890/0012-9658(2007)88[243:BTFEMA]2.0.CO;2.

Desai, A.R., Davis, K.J., Senff, C.J., Ismail, S., Browell, E.V., Stauffer, D.R., Reen, B.P., 2006. A case study on the effects of heterogeneous soil moisture on mesoscale boundary-layer structure in the Southern Great Plains, U.S.A. part I: simple prognostic model. Bound. Layer Meteorol. 119, 195 238. https://doi.org/10.1007/s10546-005-9024-6.

Elith, J., Leathwick, J.R., Hastie, T., 2008. A working guide to boosted regression trees. J. Anim. Ecol. 77, 802 813. https://doi.org/10.1111/j.1365-2656.2008.01390.x.

Emeis, S., Schafer, K., Münkel, C., 2008. Long-term observations of the urban mixing-layer height with ceilometers. IOP Conf. Ser. Earth Environ. Sci. 1, 012027 https://doi.org/10.1088/1755-1315/1/1/012027.

Eresmaa, N., Karppinen, A., Joffre, S.M., Rasanen, J., Talvitie, H., 2006. Mixing height determination by ceilometer. Atmospheric Chem. Phys. 6, 1485 1493. https://doi.org/10.5194/acp-6-1485-2006.

Findell, K.L., Eltahir, E.A.B., 2003. Atmospheric controls on soil moisture boundary layer interactions. Part I: framework development. J. Hydrometeorol. 4, 552 569. https://doi.org/10.1175/1525-7541(2003)004 0552:ACOSML 2.0.CO;2.

Fischer, M.L., Billesbach, D.P., Berry, J.A., Riley, W.J., Torn, M.S., 2007. Spatiotemporal variations in growing season exchanges of CO_2, H_2O, and sensible heat in agricultural fields of the southern great plains. Earth Interact 11, 1 21. https://doi.org/10.1175/EI231.1.

Freedman, J.M., Fitzjarrald, D.R., Moore, K.E., Sakai, R.K., 2001. Boundary layer clouds and vegetation atmosphere feedbacks. J. Clim. 14, 180 197. https://doi.org/10.1175/1520-0442(2001)013 0180:BLCAVA 2.0.CO;2.

Friedman, J.H., 2001. Greedy function approximation: a gradient boosting machine. Ann. Stat. 29 https://doi.org/10.1214/aos/1013203451.

Garratt, J., 1994. Review: the atmospheric boundary layer. Earth Sci. Rev. 37, 89 134. https://doi.org/10.1016/0012-8252(94)90026-4.

Gibert, F., Schmidt, M., Cuesta, J., Ciais, P., Ramonet, M., Xueref, I., Larmanou, E., Flamant, P.H., 2007. Retrieval of average CO_2 fluxes by combining in situ CO_2 measurements and backscatter lidar information: CO_2 FLUX. J. Geophys. Res. Atmospheres 112. https://doi.org/10.1029/2006JD008190.

Gierens, R.T., Henriksson, S., Josipovic, M., Vakkari, V., van Zyl, P.G., Beukes, J.P., Wood, C.R., O Connor, E.J., 2019. Observing continental boundary-layer structure and evolution over the South African savannah using a ceilometer. Theor. Appl. Climatol. 136 (1), 333 346. https://doi.org/10.1007/s00704-018-2484-7.

Haeffelin, M., Angelini, F., Morille, Y., Martucci, G., Frey, S., Gobbi, G.P., et al., 2012. Evaluation of mixing-height retrievals from automatic profiling Lidars and ceilometers in view of future integrated networks in Europe. Bound. Layer Meteorol 143, 49 75. https://doi.org/10.1007/s10546-011-9643-z.

Helbig, M., Gerken, T., Beamesderfer, E.R., Baldocchi, D.D., Banerjee, T., Biraud, S.C., et al., 2021. Integrating continuous atmospheric boundary layer and tower-based flux measurements to advance understanding of land-atmosphere interactions. Agric. For. Meteorol. 307, 108509 https://doi.org/10.1016/j.agrformet.2021.108509.

Hicks, M., Demoz, B., Vermeesch, K., Atkinson, D., 2019. Intercomparison of mixing layer heights from the National Weather Service ceilometer test sites and collocated radiosondes. J. Atmos. Oceanic Technol. 36 (1), 129 137. https://doi.org/10.1175/JTECH-D-18-0058.1.

Higgins, R.W., Yao, Y., Wang, X.L., 1997. Influence of the North American monsoon system on the U.S. summer precipitation regime. J. Clim. 10, 2600 2622. https://doi.org/10.1175/1520-0442(1997)010 2600:IOTNAM 2.0.CO;2.

Hollinger, D.Y., Davidson, E.A., Fraver, S., Hughes, H., Lee, J.T., Richardson, A.D., Savage, K., Sihi, D., Teets, A., 2021. Multi-decadal carbon cycle measurements indicate resistance to external drivers of change at the Howland forest AmeriFlux site. J. Geophys. Res. Biogeosciences 126. https://doi.org/10.1029/2021JG006276 e2021JG006276.

Holzworth, G.C., 1967. Mixing depths, wind speeds and air pollution potential for selected locations in the United States. J. Appl. Meteorol. 6, 1039 1044. https://doi.org/10.1175/1520-0450(1967)006 1039:MDWSAA 2.0.CO;2.

Jin, M., Dickinson, R.E., 2010. Land surface skin temperature climatology: benefitting from the strengths of satellite observations. Environ. Res. Lett. 5, 044004 https://doi.org/10.1088/1748-9326/5/4/044004.

Knauer, J., El-Madany, T.S., Zaehle, S., Migliavacca, M., 2018. Bigleaf an R package for the calculation of physical and physiological ecosystem properties from eddy covariance data. PLoS One 13, e0201114. https://doi.org/10.1371/journal.pone.0201114.

Konings, A.G., Katul, G.G., Porporato, A., 2010. The rainfall-no rainfall transition in a coupled land-convective atmosphere system: rainfall-no rainfall transition. Geophys. Res. Lett. 37 https://doi.org/10.1029/2010GL043967.

Koster, R.D., Schubert, S.D., Suarez, M.J., 2009. Analyzing the concurrence of meteorological droughts and warm periods, with implications for the determination of evaporative regime. J. Clim. 22, 3331 3341. https://doi.org/10.1175/2008JCLI2718.1.

Kotthaus, S., Grimmond, C.S.B., 2018. Atmospheric boundary-layer characteristics from ceilometer measurements. Part 1: a new method to track mixed layer height and classify clouds. Q. J. R. Meteorol. Soc. 144, 1525 1538. https://doi.org/10.1002/qj.3299.

Kotthaus, S., Haeffelin, M., Drouin, M.-A., Dupont, J.-C., Grimmond, S., Haefele, A., Hervo, M., Poltera, Y., Wiegner, M., 2020. Tailored algorithms for the detection of the atmospheric boundary layer height from common automatic lidars and ceilometers (ALC). Remote Sens. 12, 3259. https://doi.org/10.3390/rs12193259.

Lansu, E.M., Heerwaarden, C.C., Stegehuis, A.I., Teuling, A.J., 2020. Atmospheric aridity and apparent soil moisture drought in European forest during heat waves. Geophys. Res. Lett. 47 https://doi.org/10.1029/2020GL087091.

Lee, S.-J., Lee, J., Greybush, S.J., Kang, M., Kim, J., 2013. Spatial and temporal variation in PBL height over the Korean Peninsula in the KMA operational regional Model. Adv. Meteorol. 2013, 1 16. https://doi.org/10.1155/2013/381630.
Lee, T.R., De Wekker, S.F.J., 2016. Estimating daytime planetary boundary layer heights over a valley from rawinsonde observations at a nearby airport: an application to the page valley in Virginia, United States. J. Appl. Meteorol. Climatol. 55, 791 809. https://doi.org/10.1175/JAMC-D-15-0300.1.
Lee, X., Goulden, M.L., Hollinger, D.Y., Barr, A., Black, T.A., Bohrer, G., et al., 2011. Observed increase in local cooling effect of deforestation at higher latitudes. Nature 479, 384 387. https://doi.org/10.1038/nature10588.
Li, Y., Li, J., Zhao, Y., Lei, M., Zhao, Y., Jian, B., et al., 2021. Long-term variation of boundary layer height and possible contribution factors: a global analysis. Sci. Total Environ. 796, 148950 https://doi.org/10.1016/j.scitotenv.2021.148950.
Lotteraner, C., Piringer, M., 2016. Mixing-height time series from operational ceilometer aerosol-layer heights. Bound. Layer Meteorol 161, 265 287. https://doi.org/10.1007/s10546-016-0169-2.
Martucci, G., Matthey, R., Mitev, V., Richner, H., 2007. Comparison between backscatter lidar and radiosonde measurements of the diurnal and nocturnal stratification in the lower troposphere. J. Atmospheric Ocean. Technol. 24, 1231 1244. https://doi.org/10.1175/JTECH2036.1.
Mesinger, F., DiMego, G., Kalnay, E., Mitchell, K., Shafran, P.C., Ebisuzaki, W., et al., 2006. North American regional reanalysis. Bull. Am. Meteorol. Soc. 87, 343 360. https://doi.org/10.1175/BAMS-87-3-343.
Morris, V., and Winston, H.A., 2016. Laser Ceilometer CL51 Demonstration Field Campaign Report (No. DOE/SC ARM-14-042, 1254298). doi:10.2172/1254298.
Mues, A., Rupakheti, M., Münkel, C., Lauer, A., Bozem, H., Hoor, P., Butler, T., Lawrence, M.G., 2017. Investigation of the mixing layer height derived from ceilometer measurements in the Kathmandu Valley and implications for local air quality. Atmospheric Chem. Phys. 17, 8157 8176. https://doi.org/10.5194/acp-17-8157-2017.
Münkel, C., Eresmaa, N., Rasanen, J., Karppinen, A., 2007. Retrieval of mixing height and dust concentration with lidar ceilometer. Bound. Layer Meteorol 124, 117 128. https://doi.org/10.1007/s10546-006-9103-3.
Münkel, C., Schafer, K., Emeis, S., 2011. Adding confidence levels and error bars to mixing layer heights detected by ceilometer. In: Kassianov, E.I., Comeron, A., Picard, R.H., Schafer, K. (Eds.), Presented at the SPIE Remote Sensing. Prague, Czech Republic, 817708. https://doi.org/10.1117/12.898122.
Novick, K.A., Biederman, J.A., Desai, A.R., Litvak, M.E., Moore, D.J.P., Scott, R.L., Torn, M.S., 2018. The AmeriFlux network: a coalition of the willing. Agric. For. Meteorol. 249, 444 456. https://doi.org/10.1016/j.agrformet.2017.10.009.
Oliphant, A.J., Dragoni, D., Deng, B., Grimmond, C.S.B., Schmid, H.-P., Scott, S.L., 2011. The role of sky conditions on gross primary production in a mixed deciduous forest. Agric. For. Meteorol. 151, 781 791. https://doi.org/10.1016/j.agrformet.2011.01.005.
Pal, S., Haeffelin, M., Batchvarova, E., 2013. Exploring a geophysical process-based attribution technique for the determination of the atmospheric boundary layer depth using aerosol lidar and near-surface meteorological measurements: new attribution lidar-derived abl depth. J. Geophys. Res. Atmospheres 118, 9277 9295. https://doi.org/10.1002/jgrd.50710.
Panwar, A., Kleidon, A., Renner, M., 2019. Do surface and air temperatures contain similar imprints of evaporative conditions? Geophys. Res. Lett. 46, 3802 3809. https://doi.org/10.1029/2019GL082248.
Papale, D., Reichstein, M., Aubinet, M., Canfora, E., Bernhofer, C., Kutsch, W., et al., 2006. Towards a standardized processing of net ecosystem exchange measured with eddy covariance technique: algorithms and uncertainty estimation. Biogeosciences 3, 571 583. https://doi.org/10.5194/bg-3-571-2006.
Perkins, J.M., 2020. Characterizing the Atmospheric Mixed Layer During the North American Monsoon at Walnut Gulch Experimental Watershed (M.S.). The University of Arizona, Ann Arbor.
Pietersen, H.P., Vila-Guerau de Arellano, J., Augustin, P., van de Boer, A., de Coster, O., Delbarre, H., et al., 2015. Study of a prototypical convective boundary layer observed during BLLAST: contributions by large-scale forcings. Atmospheric Chem. Phys. 15, 4241 4257. https://doi.org/10.5194/acp-15-4241-2015.
Piringer, M., Joffre, S., Baklanov, A., Christen, A., Deserti, M., De Ridder, K., et al., 2007. The surface energy balance and the mixing height in urban areas activities and recommendations of COST-Action 715. Bound. Layer Meteorol. 124, 3 24. https://doi.org/10.1007/s10546-007-9170-0.
Poltera, Y., Martucci, G., Collaud Coen, M., Hervo, M., Emmenegger, L., Henne, S., et al., 2017. PathfinderTURB: An automatic boundary layer algorithm. Development, validation and application to study the impact on in situ measurements at the Jungfraujoch. Atmos. Chem. Phys. 17, 10051 10070. https://doi.org/10.5194/acp-17-10051-2017.
Ramanathan, V., Cess, R.D., Harrison, E.F., Minnis, P., Barkstrom, B.R., Ahmad, E., Hartmann, D., 1989. Cloud-radiative forcing and climate: results from the earth radiation budget experiment. Science 243, 57 63. https://doi.org/10.1126/science.243.4887.57.
Rey-Sanchez, C., Wharton, S., Vila-Guerau de Arellano, J., Paw, U, K.T., Hemes, K.S., Fuentes, J.D., Osuna, J., Szutu, D., Ribeiro, J.V., Verfaillie, J., Baldocchi, D., 2021. Evaluation of atmospheric boundary layer height from wind profiling radar and slab models and its responses to seasonality of land cover, subsidence, and advection. J. Geophys. Res. Atmospheres 126. https://doi.org/10.1029/2020JD033775.
Richardson, A.D., 2019. Tracking seasonal rhythms of plants in diverse ecosystems with digital camera imagery. New Phytol. 222, 1742 1750. https://doi.org/10.1111/nph.15591.
Ridgeway, G., 2020. Generalized Boosted Models: A guide to the gbm package. R Package.
Salcido, A., Celada-Murillo, A.-T., Carreon-Sierra, S., Castro, T., Peralta, O., Salcido-Gonzalez, R.-S., Hernandez-Flores, N., Tamayo-Flores, G.-A., Martínez-Flores, M.-A., 2020. Estimations of the Mexicali valley (Mexico) mixing height. Atmosphere 11, 505. https://doi.org/10.3390/atmos11050505.
Salvucci, G.D., Gentine, P., 2013. Emergent relation between surface vapor conductance and relative humidity profiles yields evaporation rates from weather data. Proc. Natl. Acad. Sci. 110, 6287 6291. https://doi.org/10.1073/pnas.1215844110.
Sanchez-Mejia, Z.M., Papuga, S.A., 2014. Observations of a two-layer soil moisture influence on surface energy dynamics and planetary boundary layer characteristics in a semiarid shrubland: observations of two-layer soil moisture. Water Resour. Res. 50, 306 317. https://doi.org/10.1002/2013WR014135.
Santanello, J.A., Dirmeyer, P.A., Ferguson, C.R., Findell, K.L., Tawfik, A.B., Berg, A., et al., 2018. Land atmosphere interactions: the LoCo perspective. Bull. Am. Meteorol. Soc. 99, 1253 1272. https://doi.org/10.1175/BAMS-D-17-0001.1.
Santanello, J.A., Friedl, M.A., Ek, M.B., 2007. Convective planetary boundary layer interactions with the land surface at diurnal time scales: diagnostics and feedbacks. J. Hydrometeorol. 8, 1082 1097. https://doi.org/10.1175/JHM614.1.
Santanello, J.A., Friedl, M.A., Kustas, W.P., 2005. An empirical investigation of convective planetary boundary layer evolution and its relationship with the land surface. J. Appl. Meteorol. 44, 917 932. https://doi.org/10.1175/JAM2240.1.
Schmid, P., Niyogi, D., 2012. A method for estimating planetary boundary layer heights and its application over the ARM southern great plains site. J. Atmospheric Ocean. Technol. 29, 316 322. https://doi.org/10.1175/JTECH-D-11-00118.1.
Schmiedeler, M.E., 2019. Impacts of Surface Variables on Atmospheric Boundary Layer Transport and Growth (M.S.). ProQuest Diss. Theses. University of California, Davis, Ann Arbor.
Schween, J.H., Hirsikko, A., Lohnert, U., Crewell, S., 2014. Mixing-layer height retrieval with ceilometer and Doppler lidar: from case studies to long-term assessment. Atmospheric Meas. Tech. 7, 3685 3704. https://doi.org/10.5194/amt-7-3685-2014.
Scott, R.L., Biederman, J.A., Hamerlynck, E.P., Barron-Gafford, G.A., 2015. The carbon balance pivot point of southwestern U.S. semiarid ecosystems: Insights from the 21st century drought. J. Geophys. Res. Biogeosciences 120, 2612 2624. https://doi.org/10.1002/2015JG003181.
Scott, R.L., Hamerlynck, E.P., Jenerette, G.D., Moran, M.S., Barron-Gafford, G.A., 2010. Carbon dioxide exchange in a semidesert grassland through drought-induced vegetation change. J. Geophys. Res. 115, G03026. https://doi.org/10.1029/2010JG001348.
Seibert, P., 2000. Review and intercomparison of operational methods for the determination of the mixing height. Atmos. Environ. 34, 1001 1027. https://doi.org/10.1016/S1352-2310(99)00349-0.
Seidel, D.J., Ao, C.O., Li, K., 2010. Estimating climatological planetary boundary layer heights from radiosonde observations: Comparison of methods and uncertainty analysis. J. Geophys. Res. 115, D16113. https://doi.org/10.1029/2009JD013680.
Seidel, D.J., Zhang, Y., Beljaars, A., Golaz, J.-C., Jacobson, A.R., Medeiros, B., 2012. Climatology of the planetary boundary layer over the continental United States and Europe: boundary layer climatology: U.S. and Europe. J. Geophys. Res. Atmospheres 117. https://doi.org/10.1029/2012JD018143.
Sellers, P.J., Hall, F.G., Kelly, R.D., Black, A., Baldocchi, D., Berry, J., et al., 1997. BOREAS in 1997: experiment overview, scientific results, and future directions. J. Geophys. Res. Atmospheres 102, 28731 28769. https://doi.org/10.1029/97JD03300.
Seyednasrollah, B., Young, A.M., Hufkens, K., Milliman, T., Friedl, M.A., Frolking, S., Richardson, A.D., 2019. Tracking vegetation phenology across diverse biomes using Version 2.0 of the PhenoCam dataset. Sci. Data 6, 222. https://doi.org/10.1038/s41597-019-0229-9.
Sinclair, V.A., Belcher, S.E., Gray, S.L., 2010. Synoptic controls on boundary-layer characteristics. Bound. Layer Meteorol. 134, 387 409. https://doi.org/10.1007/s10546-009-9455-6.
Siqueira, M., Katul, G., Porporato, A., 2009. Soil moisture feedbacks on convection triggers: the role of soil plant hydrodynamics. J. Hydrometeorol. 10, 96 112. https://doi.org/10.1175/2008JHM1027.1.
Sorooshian, A., Wonaschütz, A., Jarjour, E.G., Hashimoto, B.I., Schichtel, B.A., Betterton, E.A., 2011. An aerosol climatology for a rapidly growing arid region (southern Arizona): major aerosol species and remotely sensed aerosol properties. J. Geophys. Res. 116, D19205. https://doi.org/10.1029/2011JD016197.
Stull, R.B., 1988. An Introduction to Boundary Layer Meteorology. Springer, Dordrecht.
Tang, G., Zhang, Jinqiang, Zhu, X., Song, T., Münkel, C., et al., 2016. Mixing layer height and its implications for air pollution over Beijing, China. Atmospheric Chem. Phys. 16, 2459 2475. https://doi.org/10.5194/acp-16-2459-2016.
van Stratum, B.J.H., Vila-Guerau de Arellano, J., van Heerwaarden, C.C., Ouwersloot, H. G., 2014. Subcloud-layer feedbacks driven by the mass flux of shallow cumulus convection over land. J. Atmospheric Sci. 71, 881 895. https://doi.org/10.1175/JAS-D-13-0192.1.
Vick, E.S., Stoy, P.C., Tang, A.C., Gerken, T., 2016. The surface-atmosphere exchange of carbon dioxide, water, and sensible heat across a dryland wheat-fallow rotation. Agric. Ecosyst. Environ. 232, 129 140. https://doi.org/10.1016/j.agee.2016.07.018.
Wiegner, M., Madonna, F., Binietoglou, I., Forkel, R., Gasteiger, J., Gei , A., Pappalardo, G., Schafer, K., Thomas, W., 2014. What is the benefit of ceilometers for aerosol remote sensing? An answer from EARLINET. Atmospheric Meas. Tech. 7, 1979 1997. https://doi.org/10.5194/amt-7-1979-2014.
Wouters, H., Petrova, I.Y., van Heerwaarden, C.C., Vila-Guerau de Arellano, J., Teuling, A.J., Meulenberg, V., Santanello, J.A., Miralles, D.G., 2019. Atmospheric boundary layer dynamics from balloon soundings worldwide: CLASS4GL v1.0. Geosci. Model Dev. 12, 2139 2153. https://doi.org/10.5194/gmd-12-2139-2019.

Wutzler, T., Lucas-Moffat, A., Migliavacca, M., Knauer, J., Sickel, K., Sigut, L., et al., 2018. Basic and extensible post-processing of eddy covariance flux data with REddyProc. Biogeosciences 15, 5015 5030. https://doi.org/10.5194/bg-15-5015-2018.

Yi, C., Davis, K.J., Bakwin, P.S., Denning, A.S., Zhang, N., Desai, A., Lin, J.C., Gerbig, C., 2004. Observed covariance between ecosystem carbon exchange and atmospheric boundary layer dynamics at a site in northern Wisconsin. J. Geophys. Res. 109, D08302. https://doi.org/10.1029/2003JD004164.

Yi, C., Davis, K.J., Berger, B.W., Bakwin, P.S., 2001. Long-term observations of the dynamics of the continental planetary boundary layer. J. Atmospheric Sci. 58, 1288 1299. https://doi.org/10.1175/1520-0469(2001)058 1288:LTOOTD 2.0.CO;2.

Yin, J., Gao, C.Y., Hong, J., Gao, Z., Li, Y., Li, X., Fan, S., Zhu, B., 2019. Surface meteorological conditions and boundary layer height variations during an air pollution episode in Nanjing, China. J. Geophys. Res. Atmospheres 124, 3350 3364. https://doi.org/10.1029/2018JD029848.

Zilitinkevich, S.S., Tyuryakov, S.A., Troitskaya, Yu.I., Mareev, E.A., 2012. Theoretical models of the height of the atmospheric boundary layer and turbulent entrainment at its upper boundary. Atmospheric Ocean. Phys. 48, 133 142. https://doi.org/10.1134/S0001433812010148.